ABSTRACT

Title of Document: DETAILED MEASUREMENTS OF FIRE-INDUCED MIXING PHENOMENA

Thomas George Layton, Master of Science, 2014

Directed By: Associate Professor Andre Marshall, Department of Fire Protection Engineering

This study successfully validated the use of salt-water analog modeling as an effective diagnostic tool for predicting fire-induced flows. A technique was developed for taking measurements using combined Planar Laser-Induced Fluorescence (PLIF) and Particle Image Velocimetry (PIV), and results were analyzed with respect to smoke filling as well as transient ceiling layer dynamics, and turbulent mixing intensity. Data was shown to be in good agreement with theory, further validating the salt-water analogy as a tool for diagnostics, prediction, and scaling of fire phenomena.

DETAILED MEASUREMENTS OF FIRE-INDUCED MIXING PHENOMENA

By

Thomas George Layton

Thesis submitted to the Faculty of the Graduate School of the
University of Maryland, College Park, in partial fulfillment
of the requirements for the degree of
Master of Science
2014

Advisory Committee:
Associate Professor Andre Marshall, Chair
Assistant Professor Michael Gollner
Associate Professor Arnaud Trouvé

Acknowledgements

I would like to thank my advisor Dr. André Marshall for at first offering me the opportunity to perform undergraduate research under his guidance, which has culminated into this research project for my Master of Science degree. His advice and support have led me to vast new knowledge, ad this project would not be possible without him. I would like to thank Dr. Arnaud Trouve for his part in my committee, as well as the knowledge he has imparted to me throughout my studies at the University, which have been relevant in both this project and my professional endeavors. I would also like to thank Dr. Michael Gollner for serving on my committee, and for the future contributions to salt water modeling he and Pietro Maisto will be performing in my succession.

For their vast amounts of help in running these experiments, I would like to thank Fernando Raffan, Adam Goodman, Charles Chan, Gerald Kingori, Dr. Nuri Serteser, Guilhem DeRoquefeuil, Justin Worden, Dr. Paolo Santangelo, and Steffen Kahrmann. Each of whom provided useful assistance in the experimental process, and had a strong influence on these results. I want to thank the Department of Justice for funding this work as part of their grant on scale modeling in fire research, as well as my company AECOM and my colleagues Frank Murphy and Ben Casey for their generosity in funding my tuition while I was working full-time. Thank you to all my other FPE friends for your help in one way or another.

Finally, I would like to thank my parents George and Mary Layton, who have done so well in raising me and leading me to the achievement of my goals.

Table of Contents

Chapter 1: Introduction 1
1.1 Literature Review 3

1.2 Research Objectives 7

Chapter 2: Approach 8
2.1 Analytical Techniques 8

2.2 Configurations 12

2.3 Diagnostics 17

2.3.1 Camera Setup 17

2.3.2 Laser Setup 18

2.3.3 Planar Laser-Induced Fluorescence (PLIF) 19

2.3.4 Particle Image Velocimetry (PIV) 23

2.3.5 PIV Time-Series 30

Chapter 3: Results and Discussion 33
3.1 Virtual Origin and Centerline Data 33

3.2 Enclosure Smoke Filling 40

3.2.1 Blue Dye Visualization 40

3.2.2 Smoke Layer Interface 42

3.2.3 Relative Fire Size 45

3.2.4 Data Averaging 48

3.2.5 Density Difference Profiles 51

3.3 Transient Ceiling Layer Dynamics 56

3.4 Mass Entrainment 61

3.5 Subgrid-Scale Mixing Analysis 63

Chapter 4: Conclusions 68

List of Figures

Figure 1, Schematic of the source and injector. 16

Figure 2, Test setup: (1) Source tank with salt-water, (2) Injector above fresh-water tank, (3) Nd:Yag Laser, (4) Laser computer and power supply, (5) CCD cameras... 16

Figure 3, Linear curve of intensity vs. concentration for Rhodamine 6G dye...... 21

Figure 4, PIV setup diagram. 24

Figure 5, vector calculation concept with multiple passes of decreasing size. 25

Figure 6, Comparison of PIV results with different dt values (a) 5.5 ms, (b)200 ms, (c) combined, H=257 mm, U_0=0.024 m/s, t*=4.8. The white outline separates values at a velocity cutoff of 0.009 m/s (u/U_0=0.375). 32

Figure 7, Instantaneous PLIF image – unconfined plume. 34

Figure 8, Time-averaged PLIF image – unconfined plume...... 34

Figure 9, Instantaneous PIV image – unconfined plume...... 35

Figure 10, Time-averaged PIV image – unconfined plume...... 36

Figure 11, Dimensionless density difference vs. position above source, showing -5/3 power law. □ *unconfined,* ○ *confined, m*=1.25e-6,* Δ *confined, m*=2.5e-6, line=theory*..... 38

Figure 12, Dimensionless velocity vs. position above source, showing -1/3 power law. □ *unconfined,* ○ *confined, m*=1.25e-6,* Δ *confined, m*=2.5e-6,* ◊ *Young,* ◁ *Yao 110 ml/min,* ▷*Yao 165 ml/min, line=theory* 39

Figure 13, blue dye smoke filling experiment at: a) plume reaching the ceiling, b) ceiling jet reaching the wall, c) t^*=5, and d) t^*=10...... 41

Figure 14, Dimensionless smoke layer height vs. dimensionless time. □m=1.25e-6, ○m*=1.3e-5, Δ=Hagglund et.al.(Multiple fire sizes).* 42

Figure 15, (a) Blue dye overshooting behavior at t=1, 1.4, 2, and 2.3 from top to bottom, (b) Smoke layer height vs. time m*=1.3e-5 measured at x_1/H =1.2* 44

Figure 16, Plot of temperature difference vs. $z/Q^{2/5}$ from McCaffrey[43] 46

Figure 16, Valid enclosure height as a function of salt water mass flow rate based on McCaffrey's plume. 47

Figure 17, Dimensionless standard deviation plotted vs. changing cell resolution along the plume centerline. The deviation starts to increase above 0.6 D, indicating that point as a limit for scaling and LES averaging before fidelity is sacrificed.* 49

Figure 18, Comparison of averaging techniques. Thin solid line: raw data; Thick dashed line: Time averaged over 1/10τ; Thin gray dashed line: Time averaged and LES averaged; Thick solid line: Time, LES, and ensemble averaged. D/H=8.3e-3* 50

Figure 19, Dimensionless density difference for confined plume at t=7.4 and m*=1.25e-6* 52

Figure 20, θ vs. x_3/H for a) x_1/H=0; b) x_1/H=0.75, c) x_1/H=1.25. □ t^*=3.7, Δ t^*=7.4, ○ t^*=14.8; m^*=1.25e-6; ensemble averaged from 3 cases, time averaged over t^*=0.3.* 53

Figure 21, θ vs. x_3/H for a) x_1/H=0; b) x_1/H=0.75, c) x_1/H=1.25. □ t^*=3.7, Δ t^*=7.4, ○ t^*=10; m^*=2.5e-6; ensemble averaged from 3 cases, time averaged over t^*=0.3.* . 53

Figure 22, Temperature profile sketch from Zukoski for a smoke layer in an enclosure. 54

Figure 23, θ vs x_1/H for x_3/H=0.93. □ t^*=3.7, Δ t^*=7.4, ○ t^*=14.8; m^*=1.25e-6; ensemble averaged from 3 cases, time averaged over t^*=0.3.* 55

Figure 24, θ^* vs x_1/H for $x_3/H=0.93$. □ $t^*=3.7$, Δ $t^*=7.4$, ○ $t^*=10$; $m^*=2.5e\text{-}6$; ensemble averaged from 3 cases, time averaged over $t^*=0.3$. 55

Figure 25, Early dimensionless ceiling jet velocity plotted over dimensionless density difference; $m^*=1.25e\text{-}6$, case 1. 57

Figure 26, Early dimensionless ceiling jet velocity plotted over dimensionless density difference; $m^*=2.5e\text{-}6$, case 1. 57

Figure 27, Qualitative theoretical velocity within the smoke layer, from Zukoski[44] .. 58

Figure 28, Instantaneous velocity at (a) t=3.7, (b) t*=7.4, and (c) t*=14.8; $m^*=1.25e\text{-}6$, case 1.* 59

Figure 29, Late-time (t=10) velocity streamlines plotted over dimensionless density difference; $m^*=1.25e\text{-}6$, case 1; time-averaged over $t^*=1.5$.* 60

Figure 30, Instantaneous (a) and mean (b) contours of mass flux; unconfined plume. 62

Figure 31, Dimensionless mass entrainment rate as a function of height above the source. 63

Figure 32, (a) Instantaneous PLIF image with and without spatial averaging (left and right half), with mixture fraction of 0.05 outlined, and (b) close-up of 1.4 D^* wide cell along centerline at z/D^* of 29. 64

Figure 33, PDF of mixture fraction in a cell along the plume centerline over time, unconfined PLIF only case. 66

Nomenclature

D^* characteristic length scale, $D^* = (\beta_{sw}\, \dot{m}_{sw}/\rho_0\, g^{1/2}\,)^{2/5}$

Q^* dimensionless source strength for fire, $Q^* = \beta_{sw}\dot{Q}/\rho_0 c_p g^{1/2} {x_3}^{5/2}$

m^*_{sw} dimensionless source strength for salt water, $m^*_{sw} = \beta_{sw}\dot{m}_{sw}/\rho_0 g^{1/2} {x_3}^{5/2}$

u^* dimensionless velocity, $u^* = u/U_0 = u/(gH)^{1/2}(m^*_{sw})^{1/3}$

θ density difference, βY_{sw}

θ^* dimensionless density difference, $\beta_{sw} Y_{sw} {m^*_{sw}}^{-2/3}$

t^* dimensionless time, $t^* = t(g/L_{sw})^{1/2}(m^*_{sw})^{1/3}$

Gr_{sw} Grashof number for salt water, $Gr_{sw} = g\beta_{sw}\dot{m}_{salt}L^2_{sw}/\rho_0 c_p v^3$

Re Reynolds number, $Re = uD/v$

Sc Schmidt number, $Sc = v/D$

c_p specific heat capacity

C_{dye} mass concentration of dye

C_{salt} mass concentration of salt

d_i apparent particle diameter on chip, $d_i = \sqrt{(Md_p)^2 + (d_{diff})^2}$

d_p seeding particle mean diameter, $d_p = 50\mu m$

d_{diff} diffraction limited image diameter, $d_{diff} = 2.44 * f\#(M+1)\lambda$

f# focal ratio, $f\# = focal\ length/entrance\ pupil\ diameter$

g gravitational acceleration

GL camera gray level

H enclosure height above virtual origin

L characteristic length

M magnification of optical system, $M = Chip\ Size/Field\ of\ View$

t time

T_0 ambient temperature

β_{sw} volumetric expansion coefficient, $\beta_{fire} = 1/T_0$, $\beta_{sw} = 0.76$

L_{sw} characteristic length scale for salt water, D^* or H

ρ_0 density of ambient water / air

λ wavelength of incident light on particle

u	velocity
v	kinematic viscosity
Y_{salt}	salt mass fraction
z, x_1	vertical position
r, x_3	radial position
z_0	virtual origin

Chapter 1: Introduction

Fire-induced flows are a substantial and relevant part of fire protection engineering. These flows govern the growth of the fire and heat transfer and also affect everything from detection to tenability. Understanding these buoyancy-driven flows is an important factor in designing safe buildings in the event of a fire. The ability to predict these flows is especially helpful in the design of automatic sprinkler and smoke detection systems, where ceiling layer temperatures and velocities are crucial. Furthermore, accurately predicting enclosure smoke filling is important in designing smoke management systems to maintain a clear height above the heads of occupants and allow safe egress.

Many empirical and theoretical equations have been developed by Alpert[1,2], Heskestad[3,4], and others to predict these properties of the smoke layer. In addition, CFD tools such as the Fire Dynamics Simulator have been created to allow further analysis of what may occur in a fire. Physical scale modeling is also a premier tool in the prediction of fire behavior. Full-scale tests have been used to produce data for smoke filling of enclosures, and have shown that theoretical and empirical correlations hold true to theory[5,6,7.]

When using enclosures that have odd features or shapes, it becomes difficult to use correlations that were designed for simpler, typically rectangular volumes. Salt-water modeling is available as a relatively cheap way of measuring smoke filling dynamics as well as performing very detailed measurements of other phenomena related to buoyancy-induced flow. It has previously been used to model detector response

times[8], smoke movement along beamed ceilings[9], and flow in multi-compartmented environments. However, there has been a lack of validation of the salt-water model for use in predicting enclosure smoke filling. Also, testing in all previous works was performed measuring salt concentration and velocity separately. As part of a grant on scale modeling of fires funded by the U.S. Department of Justice, this project aimed to validate salt-water modeling as a viable predictor of smoke filling in an enclosure, develop a technique for combining particle image velocimetry (PIV) and planar laser-induced fluorescence (PLIF) to allow for simultaneous concentration and velocity measurements, and expand on the existing PIV & PLIF measurement techniques to produce more accurate results.

Two salt-water test configurations were used in these experiments: an unconfined plume set in the center of the large tank, and a confined plume set in a rectangular enclosure. Unconfined plume tests were used to evaluate centerline plume dynamics, mass entrainment, and sub-grid scale mixing. The confined plume tests focused on smoke filling and smoke layer dynamics, with potential applications including response times of smoke detectors and fire sprinklers. Many experiments have studied smoke layer kinematics, but few have had the ability to simultaneously measure velocity and density difference at a very high resolution. In this study, the observed phenomena will be explored in detail in the salt-water model while applying scaling laws and dimensionless parameters identified to be important in these flows.

1.1 Literature Review

Physical scale modeling of fire has been a very useful tool in all engineering fields, allowing inexpensive representation of otherwise large or complex scenarios. Many researchers have developed tools for evaluating physical scale modeling to allow various fire sizes and room geometries to be scaled and to match with full-scale fire data, with all the data collapsing. Quintiere[10] developed the techniques for Froude scaling in fire studies, where the governing equations are non-dimensionalized and the convective processes are emphasized. These same methods were used by Yao[11] to establish the analog modeling between salt-water flow and fire-induced flow.

In addition to general scaling laws, many other correlations have been developed to predict more specific fire-induced flows. Heskestad[12] developed correlations for maximum ceiling jet temperature and velocity based on alcohol pool-fire tests performed in the 1950s. He also published a paper[13] providing relations for flame heights, temperatures, velocities, concentrations of combustion products, and entrainment rates, as well as some other discussion of fire plumes. Beyler[14] also published a paper providing expressions for plume and ceiling jet flows, including the equations given by Heskestad and Zukoski. Of particular relevance to these experiments are Zukoski's[15] correlations for mean centerline temperature difference and velocity as a function of height above a point source plume. These correlations were used as one of the primary metrics for evaluating the accuracy of the salt-water modeling results.

Faeth's report for the U.S. Department of Commerce and NIST discusses fire impingement on a horizontal ceiling, and has measurements of and equations for flame heights, impinging flame lengths, ceiling heat flux, and mean temperature distribution.[16] Ceiling jet behavior is an important factor in designing automatic suppression and detection systems. There has been a large amount of work in testing ceiling jet flows, using full-scale experiments as well as computer modeling and hand calculations. Alpert[17] has done a lot of work in this field, the results of which are discussed in his *Ceiling Jet Flows* chapter of the SFPE Handbook. He has developed correlations for ceiling jet temperatures and velocities based on fire strength and room height, as well as providing equations for heat transfer to the ceiling. This project developed a technique to measure various properties of ceiling jet and smoke layer flows in high detail.

A number of experimental tests have been run to validate computer models of smoke filling as well as theoretical equations. Zukoski[18] used a mass-based approach to smoke filling with thermodynamic control volumes to develop a theoretical relationship between smoke layer height and time. Hagglund[19] performed a number of smoke filling tests of an enclosure, measuring smoke layer height and other properties. Hurley[20] used a computer model to estimate ceiling layer temperatures and smoke layer elevation to Hagglund's measurements as well as data from a smoke filling test in an abandoned Nike missile silo, with accurate results.

Cooper et al.[21] performed full-scale tests, investigating the smoke layers forming in a fire room and attached corridor to generate data for verification of mathematical models. Vertical arrays of thermocouples and photometers were used and interface

location was reported over time. Zukoski and Kubota[22] developed a zone model for smoke movement in a building, predicting motion of the interface between the layers as well as the density of the layers as a function of time.

The salt-water modeling technique has been in use for some time, using both qualitative and quantitative methods. Thomas et al.[23] explored the use of vents for removing smoke from enclosures, Tangren et al.[24] used it as a way to model smoke layer migration in a ventilated compartment, and Zukoski[25] used it to predict smoke movement within tall buildings. Steckler et al.[26] established the use of hydraulic analog scaling in salt-water modeling for comparison to fire-induced flows, and used it to model flows through a scale model of a navy ship. This project evaluated salt-water modeling in multiple configurations, to further the diagnostic techniques of blue dye smoke filling experiments as well as PIV and PLIF.

Jankiewicz8 used PLIF to measure ceiling layer concentrations and flows through a multi-compartmented enclosure, in order to study detector response times. His work was compared to full-scale tests of the same nature, and concluded that salt-water modeling accurately predicts front arrival time at various locations, and that front arrival time and detector activation lag time are better predictors of detector response than gas temperature and smoke concentration. Chan9 conducted salt-water modeling tests and compared ceiling layer flows in a complex beamed ceiling to full scale fire tests, using PLIF and PIV, and confirmed that salt-water modeling can be used for predicting front arrival times and detector response by using an activation lag time. Yao[11] measured salt-water tests in an unconfined and impinging plume configuration and compared these measurements to McCaffrey's[27] fire plume

temperature measurements, point source plume theory, and Alpert's[28] ceiling jet analysis. Young[29] used a setup with a blower to measure plume dispersion near a building in a cross-flow environment.

Previous studies unrelated to salt-water modeling have combined PLIF and PIV experiments to provide velocity and scalar measurements simultaneously. Webster *et al*[30]. used simultaneous PLIF and particle tracking velocimetry in order to measure velocity and concentration fields in a turbulent jet. It was concluded that the technique is effective for measuring mean velocity, turbulent stresses, mean concentration and variance, and turbulent flux. Lipp *et al.*[31] performed simultaneous PLIF and PIV on a turbulent shear flow as a test to validate CFD subgrid mixing models. Mixing was evaluated based on the destruction of Rhodamine WT dye by a mixture of hydrogen peroxide and ferrous ion, which destroys the flurophore in the Rhodamine. Shimura *et al.*[32] performed simultaneous dual-plane PLIF and stereo-PIV on a premixed methane flame, and were able to measure the flame front in three dimensions. 3D flame structures were measured and compared to structures shown by previous 3D direct numerical simulations of turbulent premixed flames.

Experiments have been conducted that evaluate the fluctuation of fully developed fire plumes though measuring a normalized standard deviation of dimensionless density difference along the centerline. Yao[11] measured the fluctuations of dimensionless density difference, and found a standard deviation of the mean value at the centerline. Shabbir and George[33] developed a correlation predicting a mean turbulence intensity, and George et al.,[34] Nakagome & Hirata,[35] Papanicolaou & List,[36] and Kotsovinos[37] performed similar measurements.

1.2 Research Objectives

A primary focus of this research was to further establish salt-water modeling as a legitimate technique for predicting smoke filling of enclosures, and to discover areas suitable for refinement in future experiments. This was performed using laser diagnostics in combination with a scale model enclosure. Also, advanced measurement techniques were developed that allow simultaneous measurement of density difference and velocity within the salt-water flow by combining PLIF and PIV measurements. Using these techniques, analysis was given to flow structures within the ceiling layer, plume mass entrainment rate, and turbulent mixing intensity.

The specific objectives of this research were to:

-Compare salt-water smoke filling measurements with experimental and theoretical data

-Refine current techniques for achieving accurate PIV and PLIF data

-Develop a technique for performing simultaneous PIV and PLIF measurements

-Develop a technique for taking PIV measurements in flow with a wide range of velocities

-Validate measurements by comparing plume dynamics with theory

-Evaluate smoke layer and ceiling jet velocity and density difference

-Develop a guideline for a maximum fire size for comparison in salt-water modeling

-Measure turbulent intensity through PLIF measurements and compare results to previous full-scale data

Chapter 2: Approach

A series of tests were performed to measure plume dynamics, enclosure smoke filling, smoke layer dynamics, and sub-grid scale mixing. These tests were performed in a large tank at the University of Maryland Department of Fire Protection Engineering laboratory, where an unconfined salt-water plume and confined plume in an enclosure were evaluated using various techniques. Planar Laser-Induced Fluorescence (PLIF) was used to measure salt concentration, Particle Image Velocimetry (PIV) was used to measure velocities, and blue dye was used for plume and ceiling layer visualization. The sub-grid scale mixing results were evaluated using only PLIF, as velocities were not important in the resolution scale analysis. A number of smoke filling tests were performed with only blue dye, as the scope of those tests was to visualize smoke layer height and provide clear images of the smoke filling behavior. All other tests were run using combined PIV and PLIF, to provide instantaneous concentrations as well as velocities throughout the flow field.

2.1 Analytical Techniques

These salt-water experiments are a valid scale representation of physical flows and provide velocity and concentration measurements with very high resolution, something not achievable using a full-scale fire or physical scale model and similar measurement techniques. Scaling of the salt-water plume uses dimensionless analysis on the governing conservation equations. Dimensionless groups are preserved between the scale-model and full-scale plumes. Yao derived these scaling relationships by non-dimensionalizing the governing equations and using

dimensionless parameters. Although it is impossible to preserve all of the dimensionless groups, the key groups are preserved. By maintaining turbulent flow in both full-scale and scale-models, the Reynolds number is preserved without having to be scaled as long as a reference velocity is defined. Dimensionless quantities allow easy comparison between various source strengths, spaces, and times. Yao's work[11] provides the derivation of these equations in detail, and the resulting terms are summarized below.

Conservation equations for the fire plume:

Momentum:

$$\frac{\partial u_j^*}{\partial t^*} + u_i^* \frac{\partial u_j^*}{\partial x_i^*} = -\frac{\partial p^*}{\partial x_i^*} + \frac{1}{\left(Gr_{source}^{fire}\right)^{\frac{1}{3}}} \frac{\partial^2 u_j^*}{\partial x_i^* \partial x_i^*} + \theta_T^* \cdot f_j^* \qquad 2.1$$

Energy:

$$\frac{\partial \theta_T^*}{\partial t^*} + u_i^* \frac{\partial \theta_T^*}{\partial x_i^*} = \frac{1}{\left(Gr_{source}^{fire}\right)^{1/3} Pr} \frac{\partial^2 \theta_T^2}{\partial x_i^* \partial x_i^*} + \dot{q}^* \qquad 2.2$$

Smoke mass species:

$$\frac{\partial \theta_{smoke}^*}{\partial t^*} + u_i^* \frac{\partial \theta_{smoke}^*}{\partial x_i^*} = \frac{1}{\left(Gr_{source}^{fire}\right)^{1/3} Sc} \frac{\partial^2 \theta_{smoke}^*}{\partial x_i^* \partial x_i^*} + w_{smoke}^* \qquad 2.3$$

Dimensionless terms for the fire plume are:

$$Gr_{source}^{fire} = \frac{g\beta_T \dot{Q} L^2}{\rho_0 c_p \nu^3} = \left(Re_{source}^{fire}\right)^3 Q^* \quad 2.4$$

$$Pr = \frac{\nu}{\alpha} \quad 2.5$$

$$Sc = \frac{\nu}{D} \quad 2.6$$

$$t^* = t(g/L)^{1/2}(Q^*)^{1/3} \quad 2.7$$

$$x_i^* = x_i/L \quad 2.8$$

$$Q_{fire}^* = \beta_T Q\left(\rho_0 c_p g^{1/2} L^{5/2}\right)^{-1} \quad 2.9$$

$$u_j^* = u_j(GL_{sw})^{-\frac{1}{2}}(m_{sw}^*)^{-1/3} \quad 2.10$$

$$\theta_T^* = \beta_T(T - T_0)(Q^*)^{-2/3} \quad 2.11$$

$$\theta_{smoke}^* = \beta_T Y_{smoke}\Delta H_C/\left(Y_{smoke} c_p (Q^*)^{2/3}\right) \quad 2.12$$

$$\beta_T = 1/T_0 \quad 2.1$$

Conservation equations for the salt-water plume:

Momentum:

$$\frac{\partial u_j^*}{\partial t^*} + u_i^* \frac{\partial u_j^*}{\partial x_i^*} = -\frac{\partial p^*}{\partial x_i^*} + \frac{1}{(Gr_{source}^{sw})^{\frac{1}{3}}} \frac{\partial^2 u_j^*}{\partial x_i^* \partial x_i^*} + \theta_{sw}^* \cdot f_j^* \quad 2.14$$

Salt mass species:

$$\frac{\partial \theta_{sw}^*}{\partial t^*} + u_i^* \frac{\partial \theta_{sw}^*}{\partial x_i^*} = \frac{1}{\left(Gr_{source}^{fire}\right)^{1/3} Sc} \frac{\partial^2 \theta_{sw}^*}{\partial x_i^* \partial x_i^*} + \dot{w}_{sw}^* \quad 2.15$$

Dimensionless terms for the salt-water plume are:

$$Gr_{source}^{sw} = \frac{g\beta_{sw}\dot{m}_{salt}L_{sw}^2}{\rho_0 \nu^3} = (Re_{source}^{sw})^3 m_{sw}^* \quad 2.16$$

$$Sc = \frac{\nu}{D} \quad 2.17$$

$$t_{sw}^* = t_{sw}(g/D^*)^{1/2}(m_{sw}^*)^{1/3} \quad 2.18$$

$$x_i^* = x_i/D^* \quad 2.19$$

$$m_{sw}^* = \beta_{sw}\dot{m}_{salt}\left(\rho_0 g^{1/2} L_{sw}^{5/2}\right)^{-1} \quad 2.20$$

$$u_j^* = u_j(GL_{sw})^{-\frac{1}{2}}(m_{sw}^*)^{-1/3} \quad 2.21$$

$$\theta_{sw}^* = \beta_{sw} Y_{salt}(m_{sw}^*)^{-2/3} \quad 2.22$$

$$\beta_T = 0.76 \quad 2.23$$

Past studies have shown that scaling the key groups provides a good approximation of the full-scale behavior[1,8,38]. Dimensionless parameters related to molecular diffusion can be neglected, since the molecular diffusion is relatively small compared to turbulent mixing. Good agreement has been shown between salt-water and full-scale fires when the Grashof number is larger than 10^9 and is large enough for flow to be turbulent in both unconfined and confined configurations.

2.2 Configurations

Two configurations were used in these experiments: an unconfined salt-water plume injected into a large fresh-water tank, and a confined plume injected into an acrylic enclosure with a small amount of leakage. The unconfined plume was used for measuring centerline plume dynamics and sub-grid scale mixing, and the confined plume was used to analyze ceiling layer dynamics and smoke filling. Combined PLIF/PIV images were taken for both configurations, and a number of varying salt-water flows were introduced in order to find the best salt mass fraction, dye concentration, and seeding concentration.

The large fresh-water tank has inner dimensions of 2.375 x 0.79 x 0.85 m high, large enough to fit a reasonably sized model and to allow turbulent flow ($Gr_{sw} > 10^9$), using a maximum field of view of approximately 700 mm. Before taking experimental images, the tank was cleaned and filled with filtered fresh water, using a cotton filter cartridge rated at 0.5 microns.

For unconfined plume experiments, a wall was placed in the model adjacent to the plume to suppress natural flows of the ambient water in the tank. Preliminary unconfined plume tests resulted in leaning of the plume to one side. Since flow from the plume is buoyancy-driven, this leaning behavior was independent of source injector alignment and was an issue of natural flows within the tank. The addition of this wall was found to eliminate the leaning behavior.

The enclosure model had dimensions of 95.5 x 20 x 26 cm high, with two ¼ inch holes drilled near the bottom of the two ends to account for leakage. Initial smoke filling testing found that a small amount leakage was necessary to achieve accurate results. A number of other holes were drilled in the model to accommodate a future need for more leakage, but were sealed for these experiments. All other areas were sealed except for a 2 cm gap on both sides of the injector to allow balancing of the mass within the model.

A gravity-driven source tank was used to pump salt-water into the injector. The source tank consisted of two 10-gallon HDPE tanks. A pump was used to flow water from the bottom tank to the top, and an elevated drain in the top tank kept its water level constant in order to provide a constant pressure at the injector. It also kept the dye and seeding particles mixed. Since Rhodamine 6G is sensitive to light, each tank was covered with a black trash bag to prevent light from entering. Dechlorinating agent was added to the source, as the Rhodamine dye is broken down by chlorine from the tap water. Without the agent, dye concentration was found to noticeably change over a matter of hours.

Flow from the source tank was regulated using three 1 L/min maximum-flow rotameters connected in parallel. The flowrate through each was calibrated based on salt-water and was found to be true to the markings while flowing salt-water, despite the difference in viscosity between salt and fresh water. With the available source pressure, the maximum possible flowrate out of the combined injectors was found to be 1.6 L/min, well above the flowrate chosen for the experiments. The flowrates used were 0.18, 0.36, and 1.0 L/min for the various tests.

The first injector used was a 3x3 square array of 5.6 mm inner diameter stainless steel tubes, which converged within a funnel to a 13x13 mm square opening. This injector was used for initial tests, including PLIF-only and blue dye experiments. Although these experiments as well as those by Chan[9] had success using this injector, later testing experienced an issue with bubbles forming at the injector which severely affected flow and mixing, allowing fresh water to pre-mix within the injector. Injector dye concentration was found to be on the order of 50% of the salt water in the source. The change in dimensionless density difference as a function of height also disagreed significantly with the theoretical -5/3 power law. Despite efforts to prevent bubbles from forming, the problem was persistent and the large injector was not used for the combined PLIF+PIV tests. Furthermore, with such a high mass flow rate of salt, the difference in optical density between the salt water and fresh water was causing images to blur for confined tests and resulting in less accuracy, especially for PIV results.

A singular 5.6 mm stainless tube was used for the combined PIV/PLIF tests. This injector was identical to those used by Yao and Jankiewicz, which was known to

produce clean flow with no bubbles. Before each test, the injector was purged of fresh water and air, and was quickly inserted into position for recording.

Figure 1 shows a schematic of the source setup, and ***Figure 2*** shows a photo of the test setup. ***Table 1*** below describes the setup parameters for each test in this project.

Table 1, Test matrix for salt-water modeling experiments.

Test Matrix					
Diagnostics	Blue Dye	PLIF	PIV+PLIF	PIV+PLIF	PIV+PLIF
Number of Cases Measured	4	300 frames	300 frames	3	3
Configuration	Confined	Unconfined	Unconfined	Confined	Confined
Ceiling Height [mm]	257	N/A	N/A	257	257
Injector	13x13 mm Square	13x13 mm Square	5.6 mm Tubular	5.6 mm Tubular	5.6 mm Tubular
FOV [mm]	1000	250	350	500	500
Camera	Canon 40D	Imager ProX 4M	Imager ProX 4M / ImagerIntense	Imager ProX 4M / ImagerIntense	Imager ProX 4M / ImagerIntense
Lens	50 mm f1.8	60 mm f2.8	60 mm f2.8 / 35 mm f2.0	60 mm f2.8 / 35 mm f2.0	60 mm f2.8 / 35 mm f2.0
Exposure [s]	1/125	0.008	0.008	0.008	0.008
Laser Interval *dt* [ms]	N/A	N/A	5500	9000	6000
Volumetric Flow Rate [Lpm]	1	1	0.18	0.18	0.36
Injection Velocity [mm/s]	99	99	122	122	244
Salt Mass Fraction	0.1	0.1	0.07	0.07	0.07
Characteristic Length Scale D^* [mm]	2.9	2.9	1.2	1.2	1.6
Virtual Origin (theta) [mm]	-40	-40	-0.008	-0.013	-0.011
Virtual Origin (u_3) [mm]	N/A	N/A	0.018	-0.008	0.009
Characteristic Velocity, U_0 [mm/s]				18.7	23.6
$\dot{m}_{salt}$ **[g/s]**	1.8	1.8	0.22	0.22	0.44
m^*_{sw} **[x10^6]**	12.8	N/A	N/A	1.25	2.5
Re_D	1488	1488	679	679	1358
Re_H	N/A	N/A	N/A	$7.2x10^3$	$7.2x10^3$
$Gr_{H,source}$	N/A	N/A	N/A	$8.93x10^{10}$	$8.93x10^{10}$

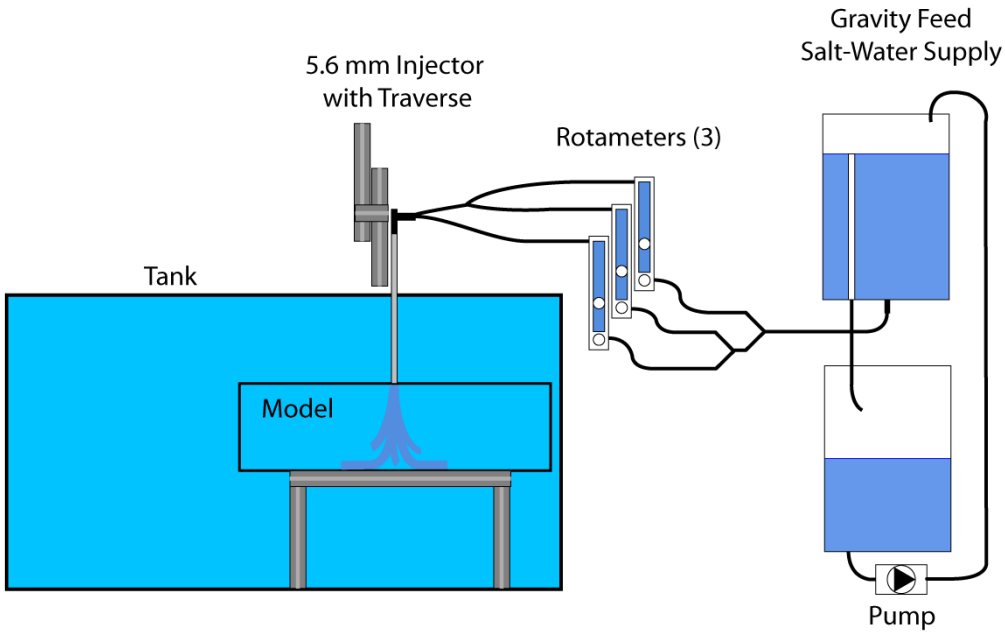

Figure 1, Schematic of the source and injector.

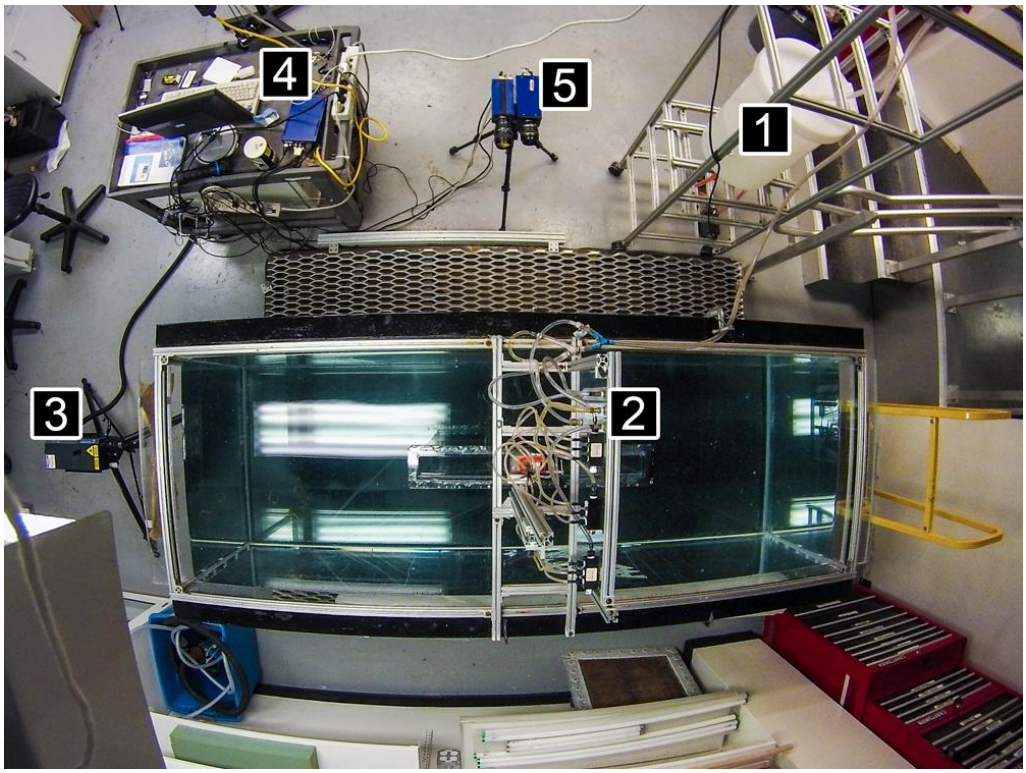

Figure 2, Test setup: (1) Source tank with salt-water, (2) Injector above fresh-water tank, (3) Nd:Yag Laser, (4) Laser computer and power supply, (5) CCD cameras.

2.3 Diagnostics

2.3.1 Camera Setup

Two cameras were used for these experiments. Combined experiments used a separate camera for PIV measurements and for PLIF measurements. The highest resolution of the two was chosen for PIV measurements, since the results of PIV post-processing are more sensitive to image quality and resolution than those for PLIF images.

The camera used for combined PIV and for single-frame PLIF tests was a LaVision ProX 4M CCD camera with a resolution of 2048 x 2048 pixels (4 megapixel), and an individual pixel size of 7.4 x 7.4 μm^2. The sensor size was 15.6 x 15.3 mm, and the max imaging frequency was 14.7 Hz, allowing the double-frame PIV images to be taken at a maximum rate of 7 Hz, though data transfer rates on the hardware limited this to 5 Hz when taking combined experiments. A Nikon 60 mm prime 1:2.8 lens and FOV of 350 mm for the unconfined plume, and a FOV of 500 mm for the confined plume. The lens was chosen based on its manually adjustable aperture, which was set to wide open for better light input. Image sharpness and depth of field were not found to be impacted by having the aperture set to wide-open.

The camera used for combined PLIF was a LaVision ImagerIntense CCD camera with a resolution of 1376(w) x 1040(h) pixels, and an individual pixel size of 6.45 x 6.45 μm^2. The camera's max imaging frequency was 10 Hz. The sensor size was 8.9 x 6.7 mm, smaller than the ProX camera's sensor, requiring a shorter focal length lens to achieve the same field of view. A Canon EF 35 mm f/2.0 lens was used to match

the horizontal field of view of the ProX with the 60 mm lens. Matching the horizontal field of view was prioritized over the vertical field of view because the enclosure model was wider than it was tall.

2.3.2 Laser Setup

The laser used was a 30 mJ double-pulse 532 nm Nd/YAG laser. It had two separate lasers firing at a set frequency with a short offset as set by the user. For PIV, the camera records one image per pulse, and with a known time between pulses, particle movement can be tracked to extract flow velocities. This time between pulses is referred to as the *dt* and has a profound effect on the quality of PIV measurements, as discussed later. For PLIF, only one pulse is necessary, with the camera recording on the first pulse only. The laser had two lenses attached, one adjusting the thickness of the laser sheet and one that spreads the circular beam into a planar sheet.

The laser was positioned as far away from the model as possible to reduce the difference in light intensity from the center of the beam to its top and bottom. Although the intensity distribution is corrected in post-processing using the sheet correction, discussed later, it is important to minimize these corrections in order to reduce error. The laser was adjusted to provide peak intensity in the center of the field of view. The optimal angle was found to be approximately 15 degrees above horizontal, appearing to point above the center of the field of view and indicating that the laser may have been due for servicing or the optics were not perfectly aligned with the beam.

2.3.3 Planar Laser-Induced Fluorescence (PLIF)

Concentration-based planar laser-induced fluorescence uses a laser sheet to illuminate a dye tracer in a fluid, with a camera recording the light intensity emitted from the dye. The intensity is linearly proportional to the concentration of the dye in the liquid. Rhodamine 6G dye was the optimum choice for salt water PLIF experiments due to its peak absorption and emission near the 532 nm wavelength of the Nd:YAG laser, as well as its resistance to photobleaching[39] and minimal sensitivity to temperature. Because of the dual camera setup, a filter was used as part of the PLIF camera optics to block 532 nm light. This blocked the light reflected off the PIV seeding particles as well as other reflective surfaces, which otherwise would ruin the measurements.

PLIF images were calibrated by first recording a background image with the laser turned off to provide a measure of the camera's dark current. The DaVis software measures light intensity in terms of "counts," and the average dark current was found to be approximately 45 counts for both cameras. This average number of counts was subtracted from all recorded images. To account for the Gaussian intensity profile of the laser sheet, a 31 x 29 x 3" calibration tank was placed into the water and filled with 0.01 mg/L of dye, enough to provide a mesaurable amount of light intensity but low enough that attenuation of the laser light over the length of the tank was negligible. A sheet image was then recorded by which the software creates a multiplier for each individual pixel and applies it to future images. This multiplier normalizes the recorded intensity based on the laser intensity distribution to provide a uniform profile.

Because the recorded data is multiplied by a value determined by the sheet image, imperfections in the sheet image can be a significant source of error. It was important to ensure the sheet image had no streaks, reflections, debris, or other visible imperfections. Common sources of streaks and imperfections were the side of the tank, the water's meniscus at the walls of the large tank and calibration tank, and objects behind the tank within the field of view. The laser sheet was masked off to prevent it from crossing the meniscus, the tank wall was thoroughly polished, and the back of the tank was covered by a white sheet. However, reflections were not able to be eliminated, so there were still some imperfections in the sheet image as well as recorded images. The model also has a hole for leakage along its centerline, so some streaks where the laser passes through the hole on the side were unavoidable. Future experiments will be necessary to find a way to eliminate reflections, and should construct a new enclosure without holes in the path of the laser.

The final step in calibrating the system was to calculate a linear function relating dye concentration to light intensity. The light intensity emitted from the Rhodamine 6G increases linearly with dye concentration, so the slope was calculated by attaching a funnel to the injector and pouring salt water from the source directly into the injector. With the dark current subtracted from the camera's readings, the slope will have an intercept at the origin, so it is only necessary to take a measurement at one concentration as well as a background measurement. To verify the linearity of the dye intensity, measurements were taken at four concentrations, diluting the source water by half for each measurement. The calibration showed excellent linearity between concentrations. ***Figure 3*** shows the results of the dye concentration

calibration for the unconfined plume test. To test the sheet correction, images were recorded flowing source water with the injector at various locations. Variations between locations were no more than 5%, which was acceptable.

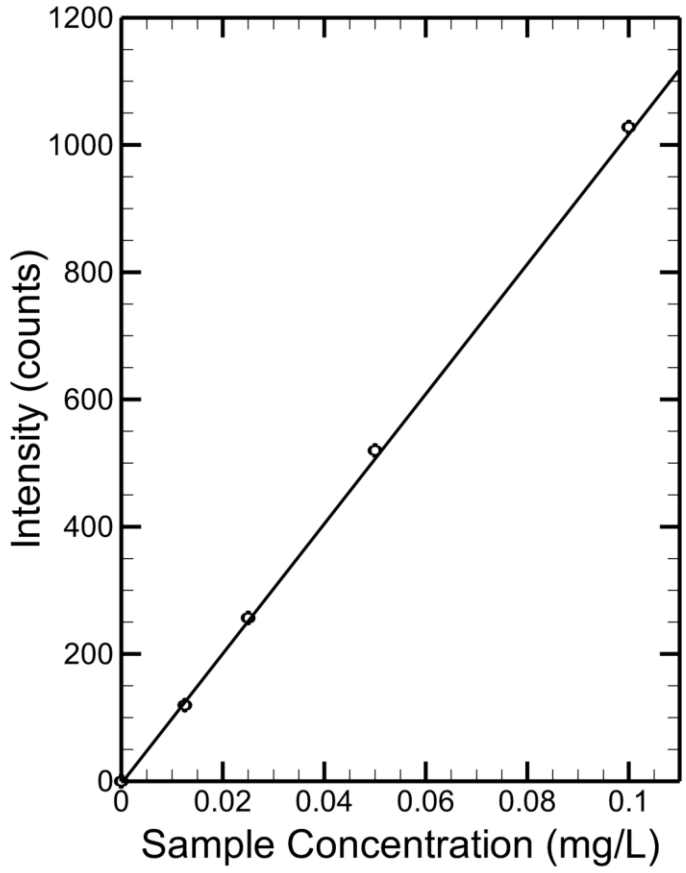

Figure 3, Linear curve of intensity vs. concentration for Rhodamine 6G dye.

Dye concentration in the source was set such that the intensity at the injector was slightly less than the maximum intensity of the camera. A dye concentration of 0.25 mg/L achieved this when laser power was set to 30% on the laser power supply's

high power mode. Preliminary PIV testing, discussed in the next section, showed that using the laser on high power produced improvement in data over low power at 100%, and a final power of 30% was chosen. Dye concentration was also kept low enough that light attenuation across the injector was less than 5%. With the small injector, no attenuation was noticed, though it was more noticeable with the large injector.

With a known injector dye concentration, salt concentration, and gray level, the salt mass fraction corresponding to light intensity can be calculated. First, a calibration coefficient relates gray level to dye mass concentration:

$$a_0 = GL/\left(C_{dye} * 1000\right) \tag{2.24}$$

The mass concentration of the dye can be calculated,

$$C_{dye} = a_1 C_{salt} \tag{2.25}$$

And the mass concentration of the salt, as defined by,

$$C_{salt} = Y_{salt}\rho_{sw} \tag{2.26}$$

With the density of salt water,

$$\rho_{sw} = (1.0 + \beta_{sw} Y_{salt})\rho_0 \tag{2.27}$$

A calibration constant relating dye mass concentration to salt mass concentration is found,

$$a_1 = C_{dye}/C_{salt} \tag{2.28}$$

Substituting the salt water density and mass concentration of salt into the equation for mass concentration of the dye,

$$\mathrm{C_{dye}} = \mathrm{a_1 Y_{salt}}(1.0 + \beta_{sw}\mathrm{Y_{salt}})\rho_0 \tag{2.29}$$

Substituting in the equation relating gray level to dye mass concentration,

$$\mathrm{GL} = \mathrm{a_0 a_1 Y_{salt}}(1.0 + \beta_{sw}\mathrm{Y_{salt}})\rho_0 \tag{2.30}$$

Solving for salt mass fraction,

$$\mathrm{Y_{sw}} \frac{=-\mathrm{a_0 a_1}\rho_0+\sqrt{(\mathrm{a_0 a_1}\rho_0)^2+4\mathrm{a_0 a_1}\beta_{sw}\rho_0 \mathrm{GL}}}{2\mathrm{a_0 a_1}\beta_{sw}\rho_0} \tag{2.31}$$

2.3.4 Particle Image Velocimetry (PIV)

A second camera was used for particle image velocimetry, where small neutrally-buoyant seeding particles within the flow are tracked over a time interval using a double-pulse laser. Velocities are found by tracking average displacement of particles throughout a number of interrogation windows over the interval between laser pulses. It is an accurate and non-intrusive quantitative method for instantaneous flow visualization. ***Figure 4*** shows the PIV setup, including the laser, light sheet, and

seeded flow. A filter was used for these tests to allow 532 nm light through and block other wavelengths.

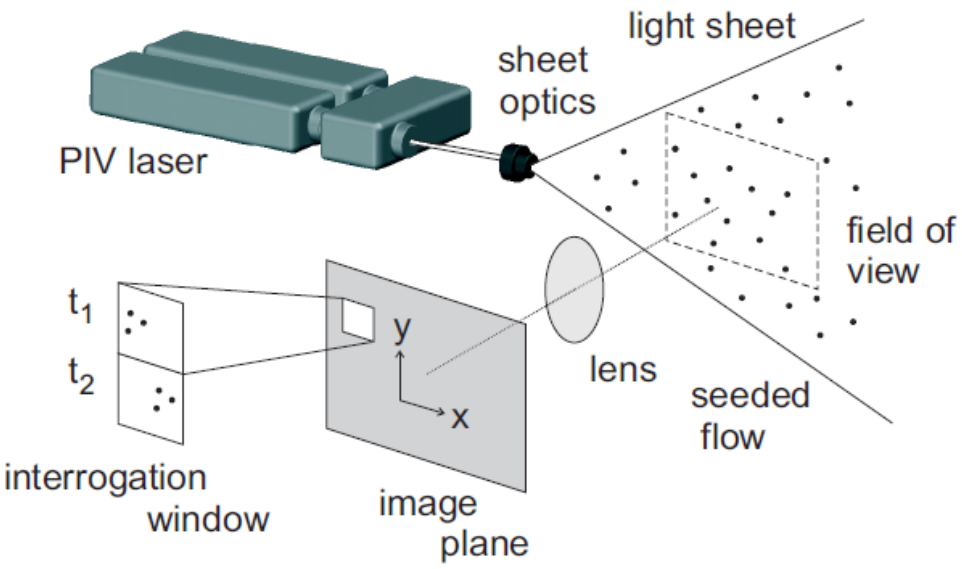

Figure 4, PIV setup diagram.

The LaVision DaVis software calculates particle velocities using a number of parameters set by the user. The software starts with a pre-processing routine that normalizes the intensity of the seeding particles and subtracts a sliding background to provide better contrast. After pre-processing, a cross-correlation method is used to track particle locations across pairs of images. A large interrogation window is initially set and the image is divided into a number of equal-sized windows. Particle locations are defined by the peak intensity of each particle image and are tracked across the time difference *dt* between frames. An initial velocity vector is found using the average particle displacement over the *dt*. This vector is then used to

provide guidance for increasingly smaller interrogation windows that provide better accuracy and resolution of the flow field. ***Figure 5*** shows this process for double-frame cross-correlation using a decreasing window size. Other options are available that use a constant size interrogation window or only a single frame with a double exposure, but these provide less accuracy. Additional information on the PIV cross-correlation method can be found in Adrian and Westerweel's book, *Particle Image Velocimetry*.[40]

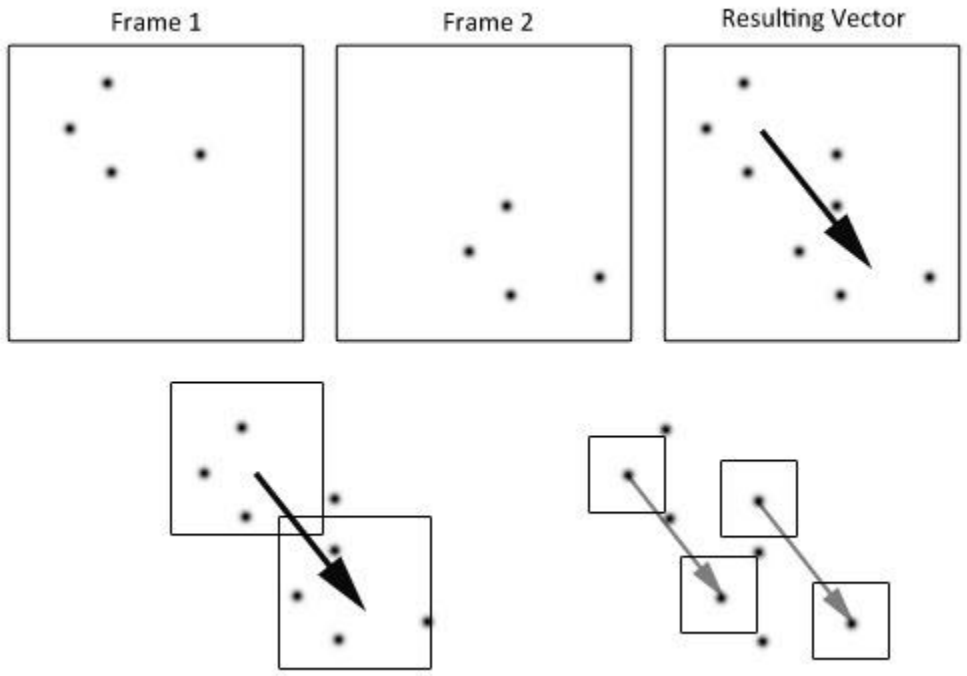

Figure 5, vector calculation concept with multiple passes of decreasing size.

PIV experiments must be designed with the post-processing in mind and must satisfy a number of design rules to achieve accurate results. Keane and Adrian[41] used Monte

Carlo simulation with varying parameters and found a set of design rules for taking optimal PIV measurements. Those rules are as follows:

The number of particles in the interrogation region shall be greater than 10:

$$N_I > 10$$

The particle image displacement shall be less than ¼ the width of the interrogation region:

$$|\Delta X| < \frac{1}{4} d_I$$

The out-of-plane displacement shall be less than ¼ the thickness of the light sheet:

$$|\Delta z| < \frac{1}{4} \Delta z_0$$

Local variation of displacements shall be less than 1/20th the size of the interrogation region:

$$M|\Delta u|\Delta t/d_I < 0.05$$

Preliminary testing was performed in order to define setup parameters such that these rules were followed. An initial interrogation region of 32x32 was set in order to provide good spatial resolution while avoiding large relative variation in displacements within each region. Larger interrogation regions sacrifice detail at the

plume edges and other areas with turbulent flow, since the region's resultant vector is the average velocity within that region.

Seeding particle type and density was determined next. Polyamide seeding particles with an average diameter of 50μm were used for seeding. These particles were chosen based on successful use in previous salt water modeling experiments by Chan9 and Young[29]. They are an excellent candidate for salt water PIV due to neutral buoyancy, good reflectivity, and a velocity response time smaller than the Kolmogorov time scale. The seeding density should be enough to provide the most particles per interrogation region before reaching a point called the speckle regime. At that point, constructive and destructive interference between light waves reflected off the particles causes the appearance of particles that do not actually exist. Once the speckle regime is reached, increasing the particle density is not noticeable, and individual particle locations are no longer being measured.

Initial testing was performed to determine the optimum seeding density. Seeding was added incrementally to the flow and images were taken to measure the difference. The flow field was fully saturated with particles at a seeding density of 60 mg/L. Beyond this point, increases in seeding density produced a diminishing effect, indicating that the speckle regime was near. The source seeding density was then set to 60 mg/L for the experiments. In order to limit attenuation of light due to high amounts of seeding in the water, the fresh water seeding was set to 1/3 that of the salt-water, 20 mg/L.

The seeding and camera should be set up such that the apparent size of the seeding particles in each image is approximately 2 pixels. Based on interpolated peak intensity between pixels, the software can determine the particle location accurate to within 0.1 pixels. If the particle image is less than or equal to one pixel, the software will encounter a "peak locking" effect, where no interpolation is possible and the displacement of pixels between frames are integer values. Apparent pixel size can be estimated using:

$$d_i = \sqrt{\left(M d_p\right)^2 + \left(d_{diff}\right)^2} \tag{2.32}$$

Where:

$$M = \frac{Chip\ Size}{Field\ of\ View} \tag{2.33}$$

$$d_p = seeding\ particle\ mean\ diameter, = 50\mu m$$

$$d_{diff} = 2.44 * f\#(M+1)\lambda \tag{2.34}$$

$f\#$ is the camera's f number or focal ratio, or the focal length divided by the diameter of the entrance pupil on the lens.

λ is the wavelength of light incident on the particle, in meters.

Calculations produced a theoretical particle size of 2 pixels. This calculation was just an estimate, and the actual images taken had an average apparent particle size of roughly double the value calculated, or 4-5 pixels. The discrepancy was most likely

due to the fact that the equation does not take into account the intensity of the laser light or glare. Using a laser power of 30% on the high power setting, apparent particle size was found to be independent from changes to the field of view and lens.

The peak locking effect is calculated by the LaVision software using a histogram of velocities, which cuts off the integer value and leaves the decimal. For example, velocities of 2.13 and 0.13 px would register as a sign of peak locking. A value of less than 0.10 is considered acceptable according to the user manual. The peak lock measured for the unconfined plume was 0.09 for PIV and 0.005 for PIV time-series. The peak lock for the plume in the confined experiments was an average of 0.003 for PIV and 0.005 for PIV time-series data in the rest of the enclosure.

Once the seeding was determined, the time between frames was set such that the maximum particle image displacement was less than ¼ the size of the interrogation region. Images were taken with various *dt* values and were processed. The maximum velocity of the resulting vectors increased until the particle image displacement was $1/6^{th}$ the width of the interrogation window, or 6 pixels. At that point, lower values of *dt* produced no noticeable change in maximum velocity. Maximum velocity was used as the metric for determining *dt* since it is set in order to eliminate dropout of vectors, which causes lower apparent velocities. The optimum displacement of 1/6 the window size was smaller than the suggested displacement of ¼, indicating that Keane and Adrian's rules are best used as a baseline and that it is important to test these parameters for new experiments.

A problem with using PIV to track the buoyancy-driven salt-water flow is the large range of velocities seen across the field of view. There is no value for *dt* that allows all particle displacements to be within the required range, so a choice is typically made as to what flows are most important. Chan used a high *dt* (50 ms) to capture the flows along the beamed ceilings, but sacrificed the plume behavior as a result9. Another option is to set the *dt* for the maximum flow observed, and sacrifice fidelity in slow moving flow. This is a reasonable compromise, because the cross-correlation processing can still provide vectors with a semblance of accuracy for slow moving flow with a short *dt*, but it cannot produce any realistic vectors for fast moving flow with a long *dt*. To resolve both fast and slow flows using normal PIV, two experiments must be made with separate *dt* values and then combined. This technique is discussed in the next section.

2.3.5 PIV Time-Series

Normal PIV processing was combined with PIV time-series processing to allow for two *dt* values to be used at once. The PIV time-series method tracks particles across two separate pairs of images, as opposed to the two frames in one pair. The *dt* for time-series is the time between pairs of images, and was set to the maximum 5 Hz (*dt*= 200 ms), limited by the ability of the hardware to record three images at a time.

The unconfined experiment *dt* value was 5.5 ms and resulted in a theoretical velocity range of 3.20 mm/s to 256 mm/s across the 350 mm field of view. The time-series velocity range for the same field of view was 0.087 mm/s to 7.03 mm/s. The

confined experiment velocity range, with a *dt* of 9000 ms and field of view of 500 mm, was 2.71 mm/s to 217 mm/s. The corresponding time-series range was 0.122 mm/s to 9.77 mm/s. Because there was good overlap in the ranges of velocity between normal PIV and PIV time-series, data sets were able to be combined based on a threshold speed above the minimum PIV velocity but below the maximum time-series velocity. Vectors in the PIV data with a speed less than the threshold are replaced with the same point from the PIV time-series data.

MATLAB was used to perform these measurements, and an outline of the threshold was added when plotting in Tecplot to visualize what data was replaced. It was found that, for the confined experiments, a threshold of 9 mm/s, or a u/U_0 of 0.375, was optimal. Lower values were more susceptible to noise in the low-velocity regions of the PIV data. The value of 9 mm/s was high enough to replace all the low velocity data without replacing vectors within the plume. For combining mean PIV and PIV time-series images, a threshold of 3 mm/s was more appropriate, as noise was minimized by time-averaging the data.

Figure 6a **and** ***b*** show the difference between a short and long *dt* for a confined plume and ceiling layer. The short 9 ms *dt* in part **a** clearly resolves the plume behavior but is very noisy elsewhere, whereas the long 200 ms *dt* in part **b** results in false vectors in the plume region, but accurate ambient and ceiling layer flow. The ambient flow is trusted to be accurate because it follows the same rules as found for the normal PIV processing, with no more than 6 pixel displacement of particles between frames. Since the PIV and PIV time-series processing algorithms are practically identical, the same rules apply even for flow velocities on a different order

of magnitude. ***Figure 6c*** shows the combined PIV and PIV time-series result for the confined plume, with a white outline separating vectors above and below u/U_0=0.375. Vector length is uniform. The plume velocities can be seen clearly, as well as the much slower entrainment into it, with seamless flow across the threshold.

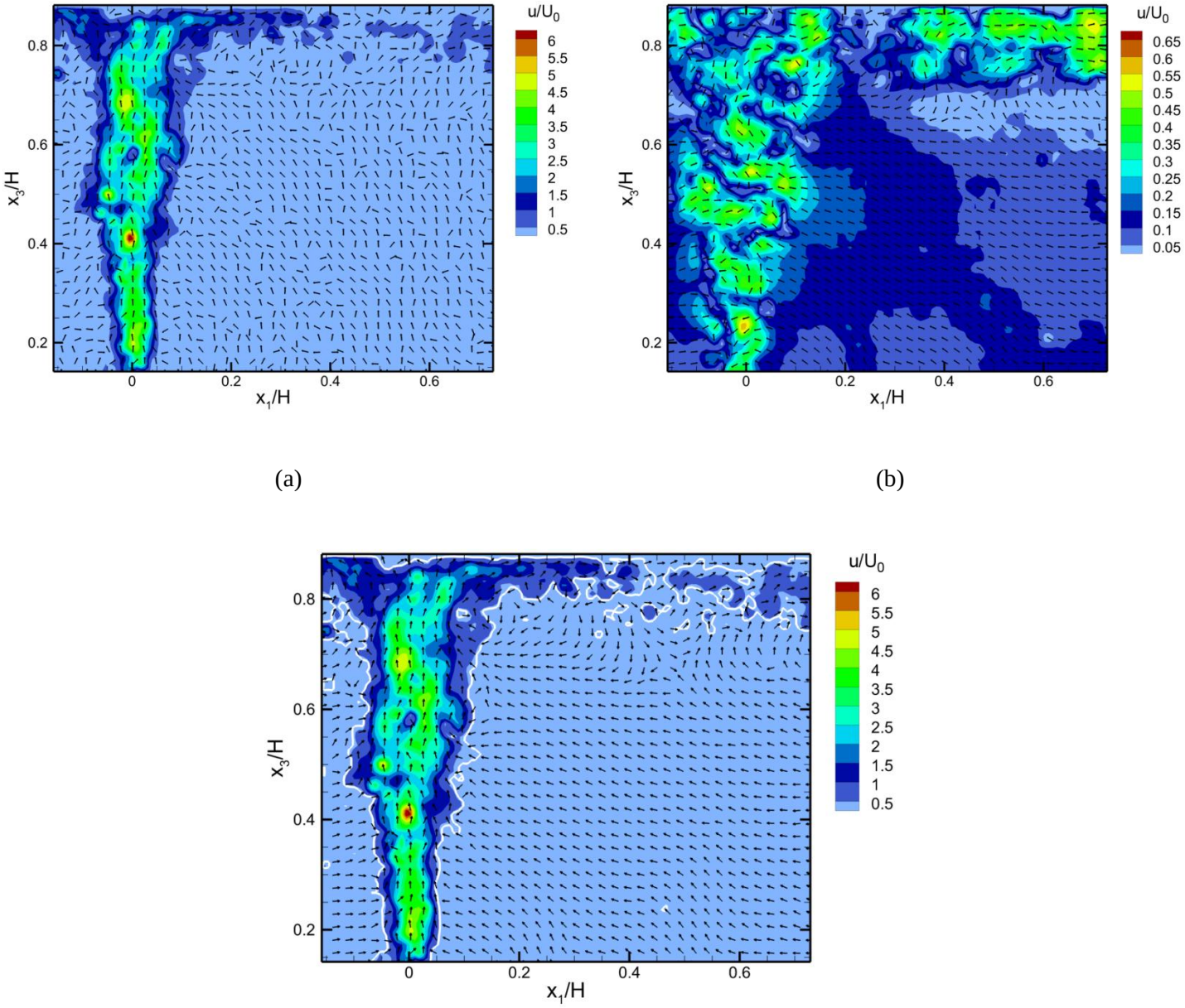

Figure 6, Comparison of PIV results with different dt values (a) 5.5 ms, (b)200 ms, (c) combined, H=257 mm, U_0=0.024 m/s, t*=4.8. The white outline separates values at a velocity cutoff of 0.009 m/s (u/U_0=0.375).

Chapter 3: Results and Discussion

Salt-water modeling experiments were performed in a variety of configurations, with the goal of advancing the current diagnostic techniques. Previous PLIF and PIV measurement techniques were expanded to provide a greater range of accuracy in measurements and to take simultaneous concentration and velocity data. These techniques were explored and analyzed from the perspective of their applicability to a variety of fire-induced flow scenarios.

3.1 Virtual Origin and Centerline Data

The unconfined plume was analyzed for a number of centerline plume characteristics. PIV and PLIF images were processed to find the plume's virtual origin, as well as centerline data that measured how well the salt-water plume conforms to theory and previous experiments. ***Figure 7*** and ***Figure 8*** show instantaneous and mean PLIF images of the unconfined plume. No abnormalities were seen in these images, where past tests showed some leaning of the plume, a steep intensity gradient due to light attenuation across the injector, and noise. These issues were resolved by following the setup parameters discussed in Chapter 2.

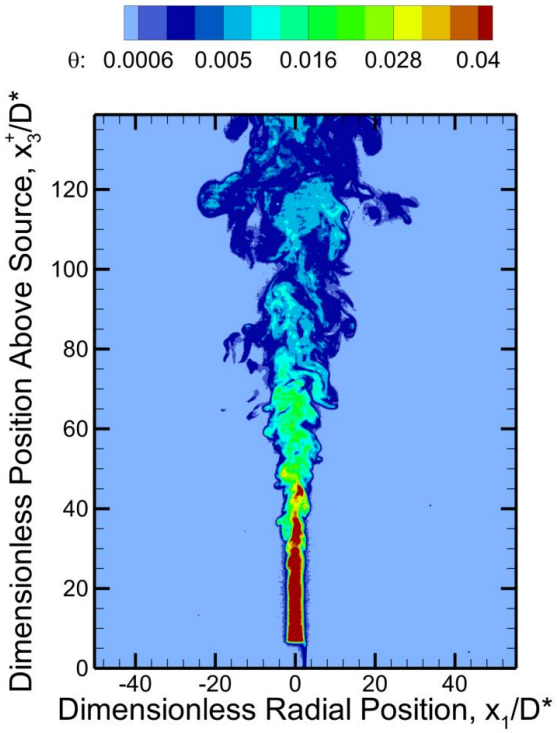

Figure 7, Instantaneous PLIF image – unconfined plume.

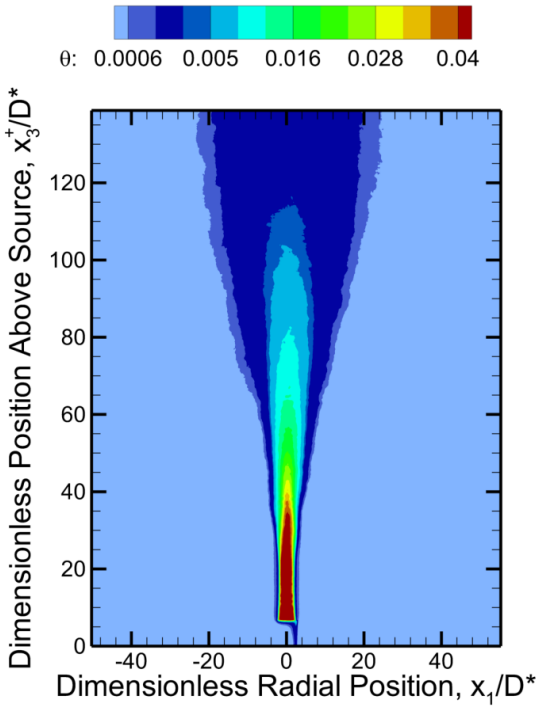

Figure 8, Time-averaged PLIF image – unconfined plume.

Figure 9 and ***Figure 10*** show instantaneous and mean PIV images of the unconfined plume. Mean centerline velocities were vertical, but the far-field velocities in the fresh water were not as expected. Typically, these vectors are expected to be perpendicular to the plume, but were measured to be in a number of directions. This was likely caused by too short of a period between mixing the seeding particles in the fresh water and running the experiment. With a wall bordering both sides of the plume, it is less likely that this was a result of natural flows within the tank. These particles are moving slowly, and were overlooked during the test setup as the PIV setup process focused almost entirely on the normal PIV tests, which do not measure these slow-moving particles. Future experiments should include running preliminary PIV time-series tests to ensure background flow is quiescent, as well as to characterize the natural currents flowing through the tank.

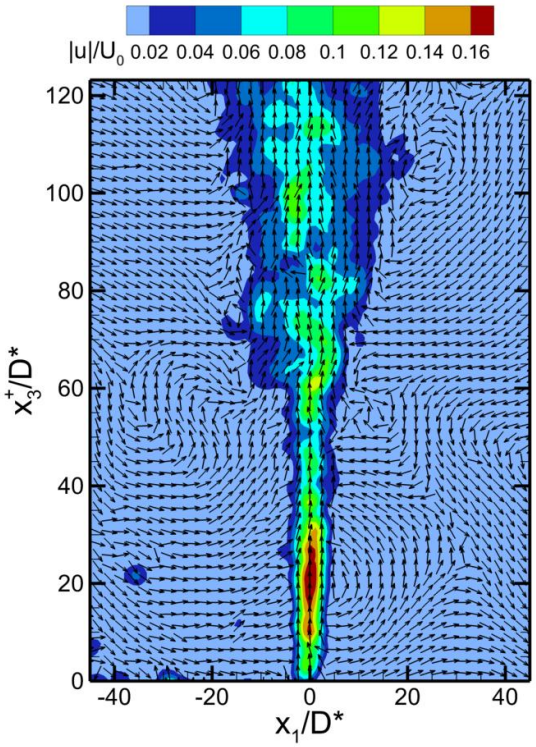

Figure 9, Instantaneous PIV image – unconfined plume.

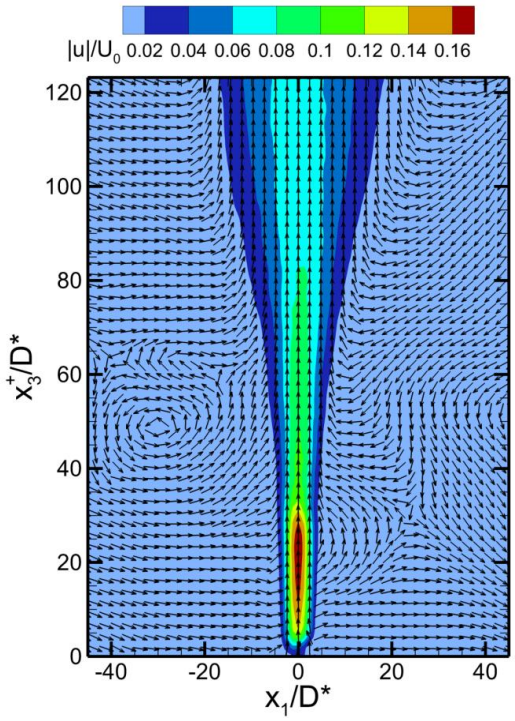

Figure 10, Time-averaged PIV image – unconfined plume.

An analysis of the centerline behavior of this plume was performed to validate the measurements being recorded. By defining the centerline density difference as $\theta^* = \theta_T/(Q_H^*)^{2/3}$, it is expected that it will equal 9.11 at x_3/H=1, because of the relation between θ_T and Q^*: $\theta_T = 9.11\, Q^{*2/3}$ as found by Zukoski[44]. For these experiments, this density difference was plotted and a curve-fit algorithm in MATLAB was used to find the experimental constant of proportionality. The constant for the unconfined experiment was found to be 9.99, and for the confined experiments was an average of 9.16.

In order to accurately plot x_3^+/D^*, the virtual origin was found by plotting x_3 vs. $(\beta Y_{sw})^{-3/5}\left(\frac{\dot{m}_{salt}}{\rho g^{\frac{1}{2}}}\right)^{2/5}$. The x-intercept of this plot was the virtual origin. This was found to be -8 mm for the unconfined test, -13 mm on average for the low-flow confined tests, and -11 mm on average for the high-flow confined tests. Yao's virtual origins were found to be on the same order, though with a positive virtual origin for the impinging plume, whereas these tests were consistently negative for both unconfined and confined configurations. Yao's values were -11.8, -18.5, and 10.2 for three of his tests, with D^*=1.33, 1.55, and 1.33 mm for each respective result. Velocity virtual origin in these experiments was also found from centerline velocity using PIV data, but was much less consistent, with values ranging between 25 and -24 mm. For the purpose of this analysis, the scalar virtual origin has been used and the velocity virtual origin disregarded.

As a test for the accuracy of the data, the centerline mean dimensionless density difference was plotted as a function of the dimensionless distance above the source. This data is expected to fit a -5/3 power, evident when plotted on a logarithmic scale[44]. All three curves precisely matched the theoretical -5/3 power law, as shown in ***Figure 11***.

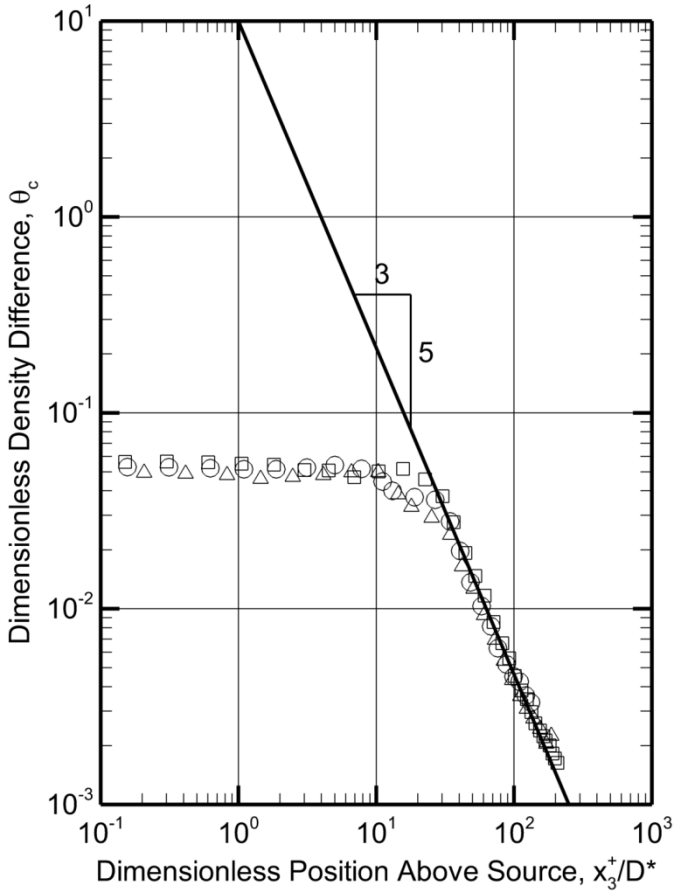

Figure 11, Dimensionless density difference vs. position above source, showing -5/3 power law. □ unconfined, ○ confined, m=1.25e-6, Δ confined, m*=2.5e-6, line=theory*

Another test to determine validity of data is to plot dimensionless velocity, $(u_3)_c/(gD^*)^{1/2}$, against dimensionless position above the source on a logarithmic scale and compare to a -1/3 power law, as found by Zukoski[44], with $u/\sqrt{gD^*} = 3.87m^{*1/3}$.

Data was averaged in the same manner as in ***Figure 11***, with ensemble averaging over the low-flow enclosed tests as well as the high-flow enclosed tests. ***Figure 12*** shows the data from these experiments overlaid with the theoretical -1/3 power curve, Yao's data and Young's data. These curves were found to conform to the -1/3 power law,

but with a slight offset to the theoretical curve. The constant of proportionality was found to be 3.37, lower than the theoretical value of 3.87. Yao's data showed a better match with the theory, and Young's data was offset opposite the data from this project. Future research should attempt to discover the cause of these inconsistencies between experiments, which may be related to the variation in velocity virtual origins as well.

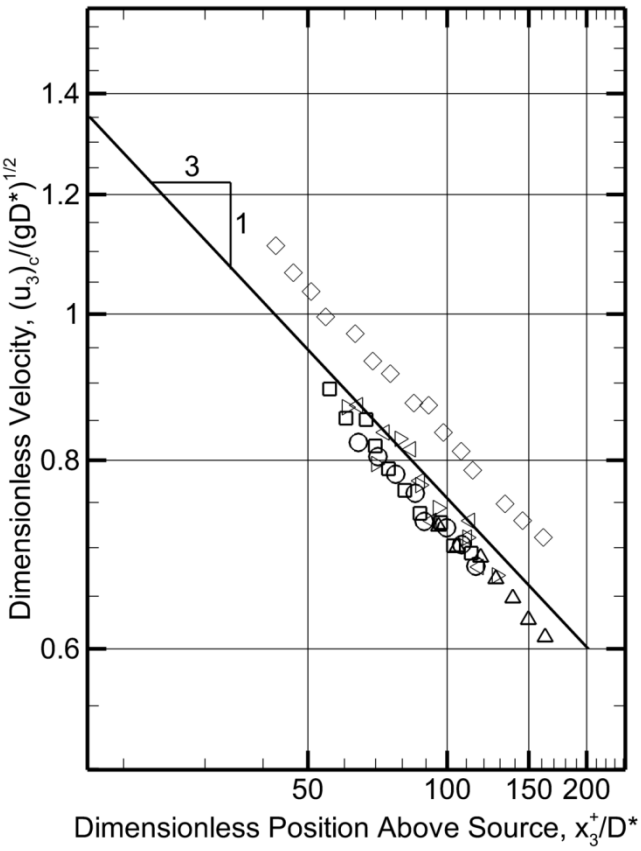

Figure 12, Dimensionless velocity vs. position above source, showing -1/3 power law. □ unconfined, ○ confined, m=1.25e-6, Δ confined, m*=2.5e-6, ◊ Young, ◁ Yao 110 ml/min, ▷Yao 165 ml/min, line=theory*

3.2 Enclosure Smoke Filling

A number of experiments were performed to measure the effectiveness of salt-water modeling in predicting enclosure smoke filling. Four images from the blue dye experiment are shown in ***Figure 13***, at four key times in the smoke filling experiment. Image results are inverted vertically in these results for the comparison to the buoyant fire plume gases in a real scenario, which rise rather than sink. Dimensionless smoke layer height at a fixed x_1/H location was measured for a number of tests and compared to theoretical data in ***Figure 14***. The repeatability of the salt-water smoke filling experiments was evaluated in ***Figure 15***, showing little variation between tests at a particular m^* value and demonstrating excellent consistency.

3.2.1 Blue Dye Visualization

A blue dye test was run to provide a visual representation of the transient ceiling jet flows within the enclosure. This test was used because the blue dye provides excellent clarity at the smoke layer interface. ***Figure 13*** shows the blue dye test, run with $D^*/H=10^6$, for a time up to $t^*=10$. The times shown are the transport lag for the plume to reach the ceiling, the transport lag for the ceiling layer to reach the wall, the time $t^*=5$, and time $t^*=10$. By the time $t^*=10$, the enclosure is filling slowly and quite steadily, with laminar flow throughout the ceiling layer.

The source was a steady-state flow of salt water at 1 L/min, corresponding to $m^*=1.28e\text{-}5$. As the ceiling jet reached the wall, a wave moved through the smoke layer, travelling between the wall and plume. This wave oscillated multiple times for up to a time of $t^*=5$, after which the smoke layer thickness was uniform. The

oscillation of the smoke layer interface height can be clearly observed in ***Figure 13c***. This is also reflected in the graph of smoke layer height vs. time, ***Figure 14***, producing points that appear to be outliers but are rather just a representation of the wave motion of the smoke layer. This behavior was repeatable between tests, as shown by ***Figure 15.***

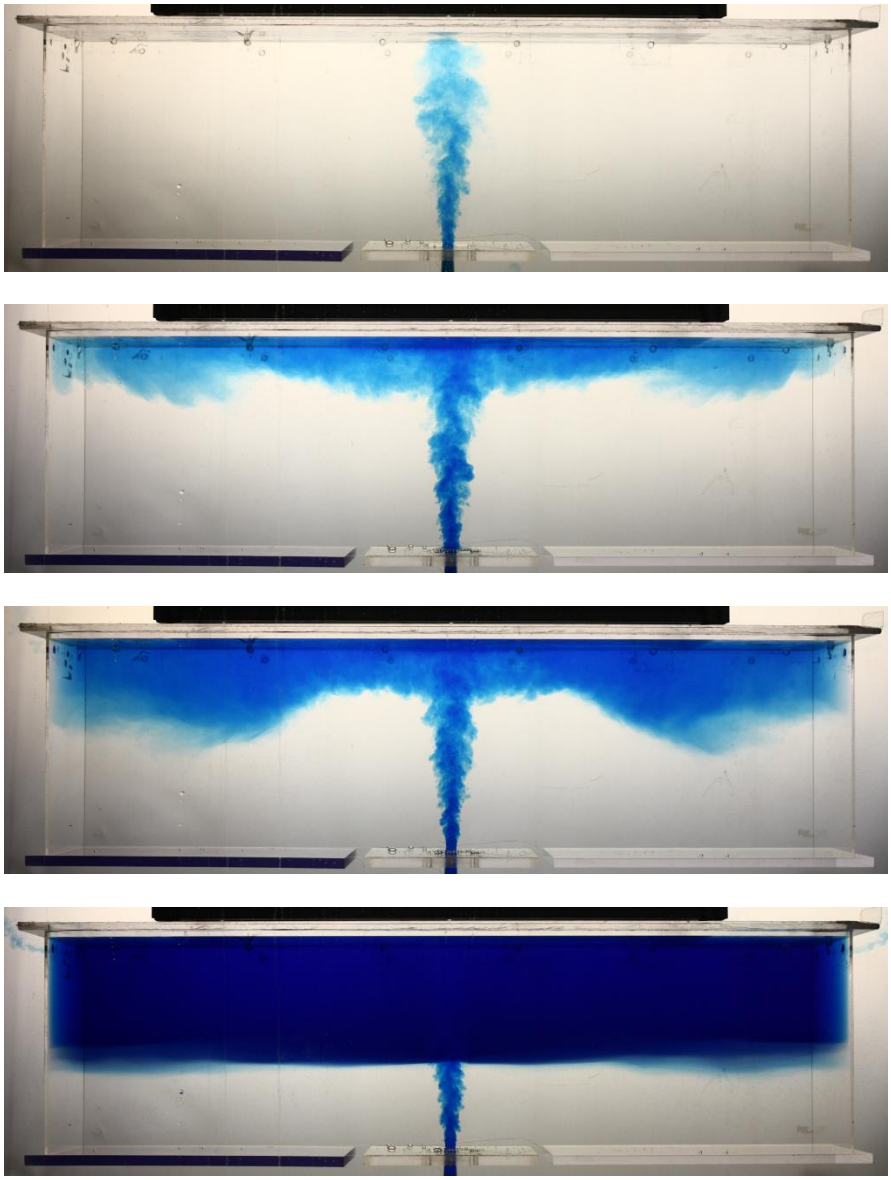

a)

b)

c)

d)

Figure 13, blue dye smoke filling experiment at: a) plume reaching the ceiling, b) ceiling jet reaching the wall, c) t^*=5, and d) t^*=10.

3.2.2 Smoke Layer Interface

Figure 14 shows the smoke layer height x_3 divided by the room height H over the dimensionless time, t^*. This data was plotted for the source strengths used: m^*=1.25e-6 for the combined PIV and PLIF experiments, and m^*=1.28e-5 for the PLIF-only and blue dye experiments. The data was compared to the theoretical results developed by Zukoski[42] for ceiling layer descent in a leaky compartment which, in turn, have been well compared to experimental data[43]. Hagglund et. al. performed full-scale smoke filling tests in a 6.15 m high enclosure using heat release rates of 30, 195, and 420 kW[19]. The smoke filling data from these tests was also plotted in ***Figure 14***, and agrees well with both the theoretical curve as well as the salt-water modeling results.

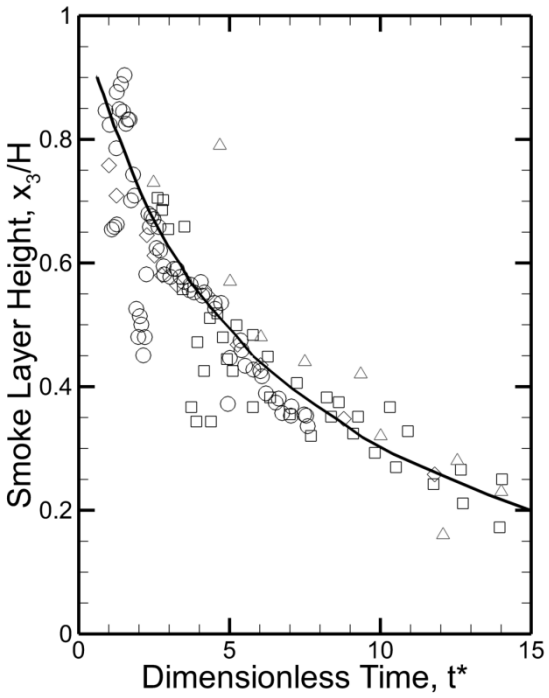

Figure 14, Dimensionless smoke layer height vs. dimensionless time. □m=1.25e-6, ○m*=1.3e-5, Δ=Hagglund et.al.(Multiple fire sizes).*

There are some outlying points among the salt-water data, but these are a result of overshooting of the smoke layer as it reaches the walls and turns[44]. Heskestad describes this behavior as "hydraulic jump."[45] ***Figure 15*** shows the smoke layer height vs. time for both tests. The overshooting of the smoke layer in the early times can be clearly seen at the beginning of each test. It can also be seen in ***Figure 13*****c**. Zukoski attributes this behavior to high ceiling jet momentum and density difference between the jet and the ambient fluid. The ceiling jet hits the wall and a stagnation point is formed at the corner which directs the jet downward, resulting in a deeper smoke layer near the wall. In these experiments, the momentum of the fluid caused the overshooting behavior to act like a wave and oscillate between the plume and wall. These oscillations ended at around t*=3 for the test with m*=1.3e-5, and ended near t*=5 for the tests with m*=6e-6.

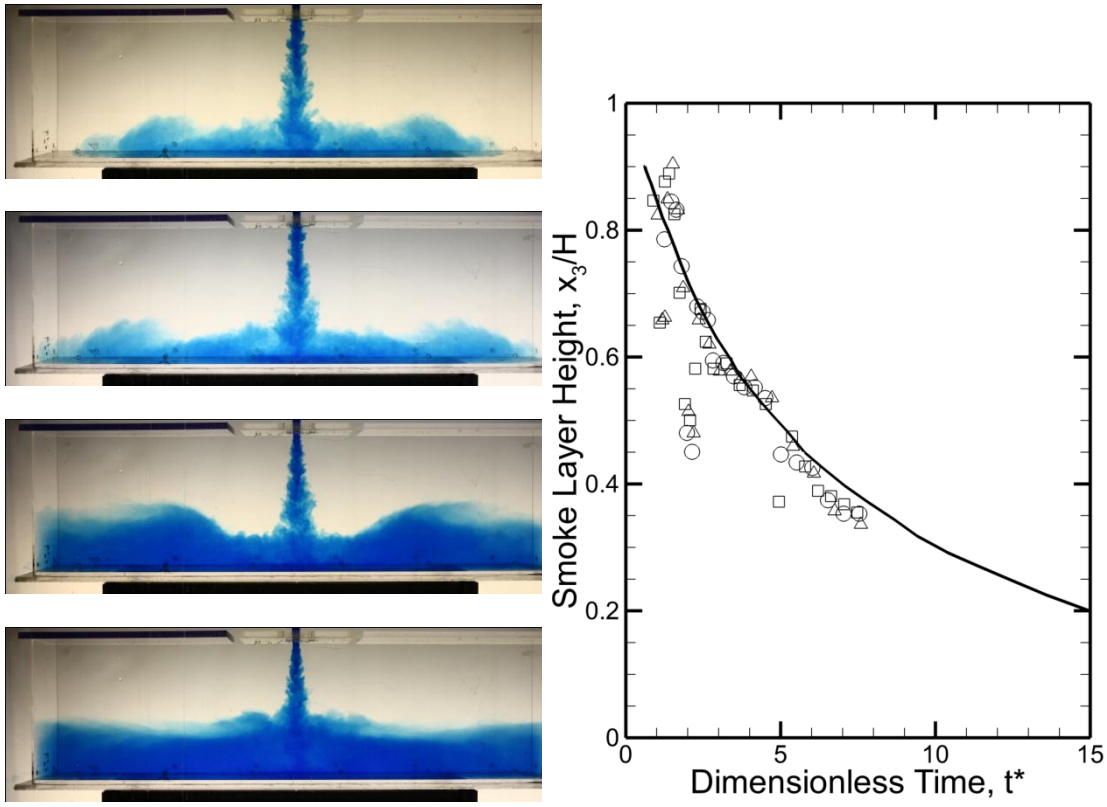

a) b)

Figure 15, (a) Blue dye overshooting behavior at t=1, 1.4, 2, and 2.3 from top to bottom, (b) Smoke layer height vs. time m*=1.3e-5 measured at x_1/H =1.2*

The oscillations occur at nearly identical times and from then on the smoke filling is consistent with the theory. Previous tests that had the salt-water source start injecting more gradually, such as those run by Kingori[46], also exhibited this behavior but the amount of overshoot was not as large and was more akin to what would be seen in a real fire where ceiling jet momentum is lower when compared to room size. However, the gradual increase in source strength at the beginning makes it much harder to develop a starting point in time as well as some dimensionless parameters, which are derived for a constant source/fire strength. Repeatability would also have been affected between experiments, making it very difficult to ensemble average

multiple tests as was performed in this project. This jump was also less prevalent for the combined PIV/PLIF experiments, which had a much lower injection flowrate.

3.2.3 Relative Fire Size

The salt-water modeling analogy is limited to small fires relative to the room size, and a maximum room fire size was established based on data from Zukoski. The relative fire size with respect to the room is best described using the dimensionless length scale of the fire, D^*. To establish this for a fire, the dimensionless source strength Q^* is set equal to 1, and the characteristic length L is extracted out of the equation. This leaves:

$$D^* = L = \left(\dot{Q}/\rho c T g^{1/2}\right)^{2/5}$$

A characteristic fire length scale with respect to the room's length scale is then established as D^*/H. Through algebra, it can be found that:

$$(D^*/H)^{5/2} = Q_H^* = m_{sw}^*$$

It may be best to refer to the fire size and salt-water strength in terms of D^*/H, since it is easier to visualize this as a ratio of length scales, rather than a Q^* or m^* value.

McCaffrey developed a figure plotting temperature differences vs. $z/Q^{2/5}$. This plot is shown in ***Figure 16***. Since salt-water modeling only models the plume and not the actual flame, the only area where the salt-water plume is accurate is for the plume region of the figure, or $z/Q^{2/5} > 0.2$.

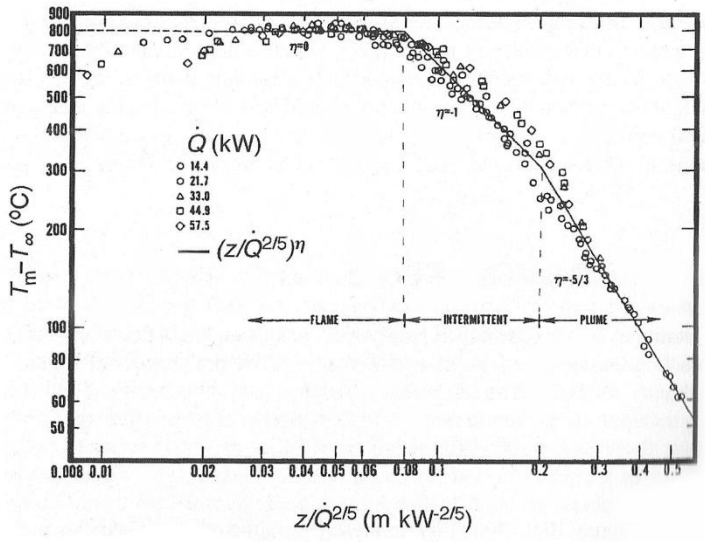

Figure 16, Plot of temperature difference vs. $z/Q^{2/5}$ from McCaffrey[43].

To present this region in a more applicable format, $z/Q^{2/5} > 0.2$ was converted to a function of D^*,

$$z/D^* > 0.2\left(\rho_0 c_p T_0 g^{1/2}\right)^{2/5}$$

Evaluating the terms on the right gives,

$$z/D^* > 3.3$$

In terms of the salt-water model, this equation can then be simplified to remove the constants,

$$z > 3.3\left(\dot{m}_{sw}\beta_{sw}/\rho_0 g^{1/2}\right)^{2/5}$$

By substituting the values for the constants, a rule is found for minimum valid enclosure size as a function of salt mass flow rate,

$$z > 0.12\ (\dot{m}_{sw})^{2/5}$$

Figure 17 shows a plot of this rule, illustrating the acceptable region of enclosure height as a function of the salt water mass flow rate.

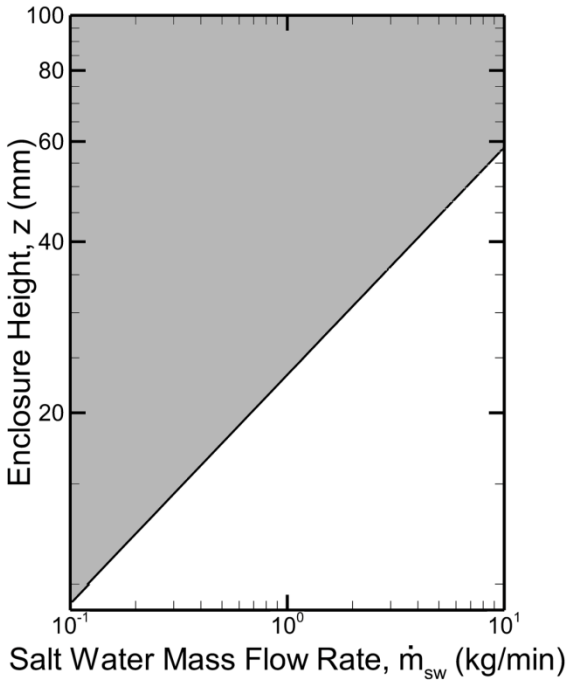

Figure 17, Valid enclosure height as a function of salt water mass flow rate based on McCaffrey's plume.

The experimental configurations used for this project were within the acceptable region as calculated herein, and also as evidenced by the plume behavior following the appropriate power laws for centerline density difference and velocity.

3.2.4 Data Averaging

An analysis into data averaging was performed to provide guidance into a resolution where LES averaging causes significant loss of fidelity in measurements. PLIF Images were post-processed using LaVision's DaVis software to calculate the dye concentration based on light intensity recorded by the camera. MATLAB was then used to process these images and convert the dye concentration into a salt mass fraction and then to a dimensionless density difference, θ^*. These images were then averaged temporally, spatially, and ensemble averaged between experiments. The results of these averaging techniques were compared in ***Figure 19***.

In the analysis of the plume and smoke layer, discussed later, the data was LES averaged to reduce noise. The largest dimension over which LES averaging would be performed was determined by analyzing the amount of turbulent fluctuation captured as the images were scaled down in resolution. Dimensionless standard deviation along the plume centerline was found and plotted in ***Figure 18***, which shows what cell resolution is required to keep fidelity in measuring turbulent fluctuations within the flow. After averaging, θ^* was plotted against x_3/H in ***Figure 21*** for three x_1/H locations and over three times. θ^* was plotted against x_1/H in ***Figure 24*** to show radial changes in density difference near the ceiling.

The standard deviation was observed to remain constant until the resolution became larger than 0.6 D^*, where it started to dramatically increase. Based on this result, a limit for LES averaging performed in this analysis was set at 0.6 D^* to avoid sacrificing fidelity.

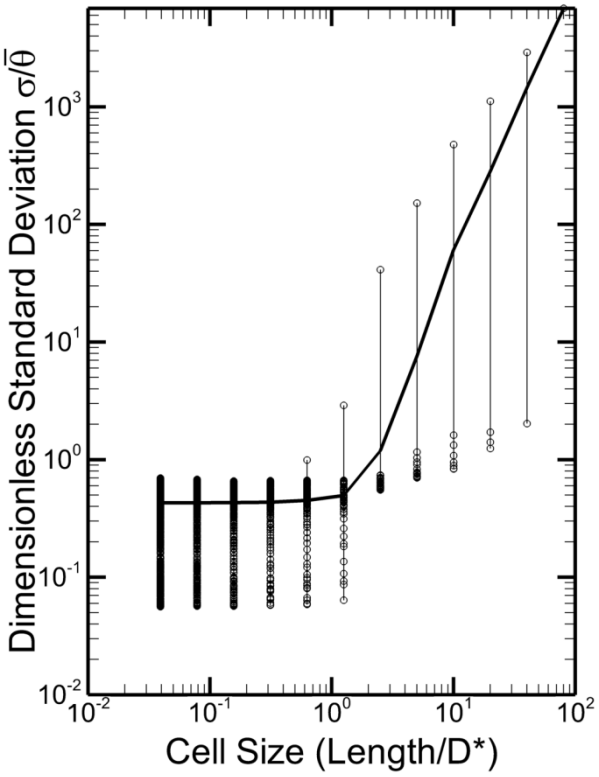

Figure 18, Dimensionless standard deviation plotted vs. changing cell resolution along the plume centerline. The deviation starts to increase above 0.6 D, indicating that point as a limit for scaling and LES averaging before fidelity is sacrificed.*

Other forms of averaging were also applied. Time averaging was used first, with a semi-arbitrary limit of 1/10 τ and was performed using the LaVision software. The limit of 1/10 τ is short enough to avoid any significant changes in the ceiling layer's transient behavior. After time averaging, LES spatial averaging was applied as mentioned previously. Ensemble averaging was used last to provide a measure of average behavior over six identical tests. ***Figure 19*** compares the different averaging techniques.

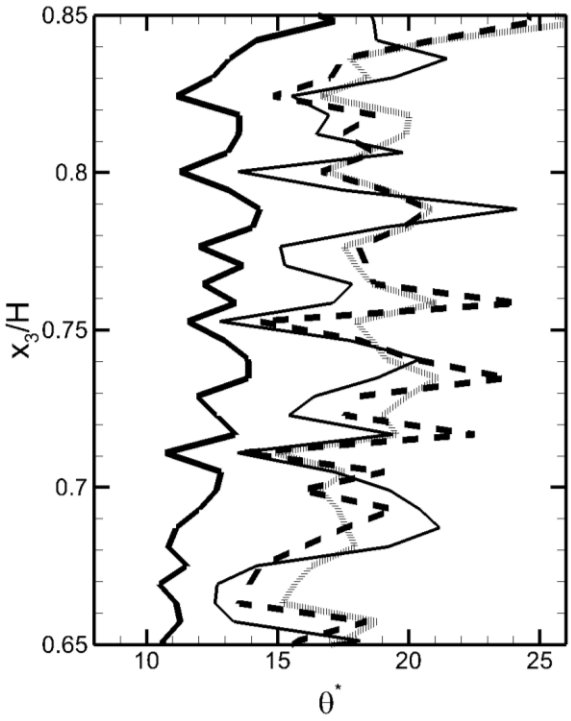

Figure 19, Comparison of averaging techniques. Thin solid line: raw data; Thick dashed line: Time averaged over 1/10τ; Thin gray dashed line: Time averaged and LES averaged; Thick solid line: Time, LES, and ensemble averaged. D/H=8.3e-3*

The instantaneous image with no averaging applied is represented by the thin solid line, and has many large peaks from noise in the data. The position used for this profile was x_1/H=1.25, and the time used was t^*=10. The thick dashed line shows data that has been time-averaged over 1/10 τ, which corresponded to 5 frames for images recorded at 7 Hz. The flow in this region was slow, so time-averaging had only a small effect. LES spatial averaging was applied next, and is shown by the thin dashed line. This averaging was much more effective in reducing noise. The most significant change was seen after ensemble averaging, since the concentration values between tests were somewhat inconsistent at this value of t^*. The amount of noise

present was not significantly changed when compared to the LES averaged data, but the mean θ^* value was shifted closer to 11 from 17.

3.2.5 Density Difference Profiles

The dimensionless density difference was calculated for the enclosed plume and plotted for the purpose of analyzing the smoke layer salt concentration. In this analysis, the density difference θ, is normalized by the dimensionless source strength m^*, and is represented as θ^*. ***Figure 20*** shows a contour plot of the density difference at t^*=7.4. Two issues to note with this image are the reflection of the plume off the back of the tank at x_1/H=0.25, as well as the visible holes in the enclosure at x_3/H=0.95. Attempts were made to eliminate reflections off the back of the enclosure, but were unsuccessful. The reflection is acceptable in this analysis, as the data from the region of the reflection is not of particular value. Future experiments should explore methods for eliminating the reflection off the back of the tank. The holes in the enclosure do affect the analysis of this data, so the profiles taken were carefully positioned to avoid the holes, as they would show up as peaks along each profile. A hole is also present on the side of the model, in the path of the laser, which causes some streaks. Future experiments should use a new enclosure model that does not have holes in the field of view or path of the laser.

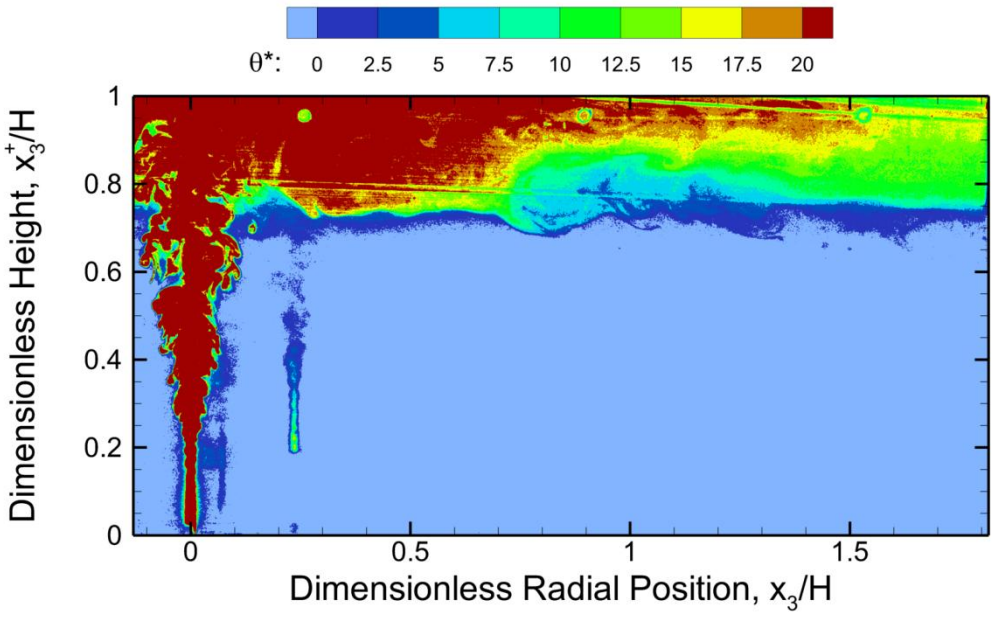

Figure 20, Dimensionless density difference for confined plume at t=7.4 and m*=1.25e-6*

The vertical profiles in ***Figure 21*** and ***Figure 22*** show vertical profiles of the plume centerline and smoke layer density difference. ***Figure 21*** shows the profiles for the low flow case, with $m^*=1.25e\text{-}6$, and ***Figure 22*** shows the high flow case, with $m^*=2.5e\text{-}6$. For both cases, the three tests per case were ensemble averaged and time-averaged over a time of $t^*=0.3$. No LES averaging was performed for these profiles. Profiles extracted from earlier experiments were noisy due to streaks and visible seeding particles, but the experimental techniques developed as part of this project were able to eliminate much of the noise and produce clean images. As a result, a linear increase in density difference from the ceiling layer interface to the wall can be observed. This is different from the temperature profile presented by Zukoski, shown in ***Figure 23***.

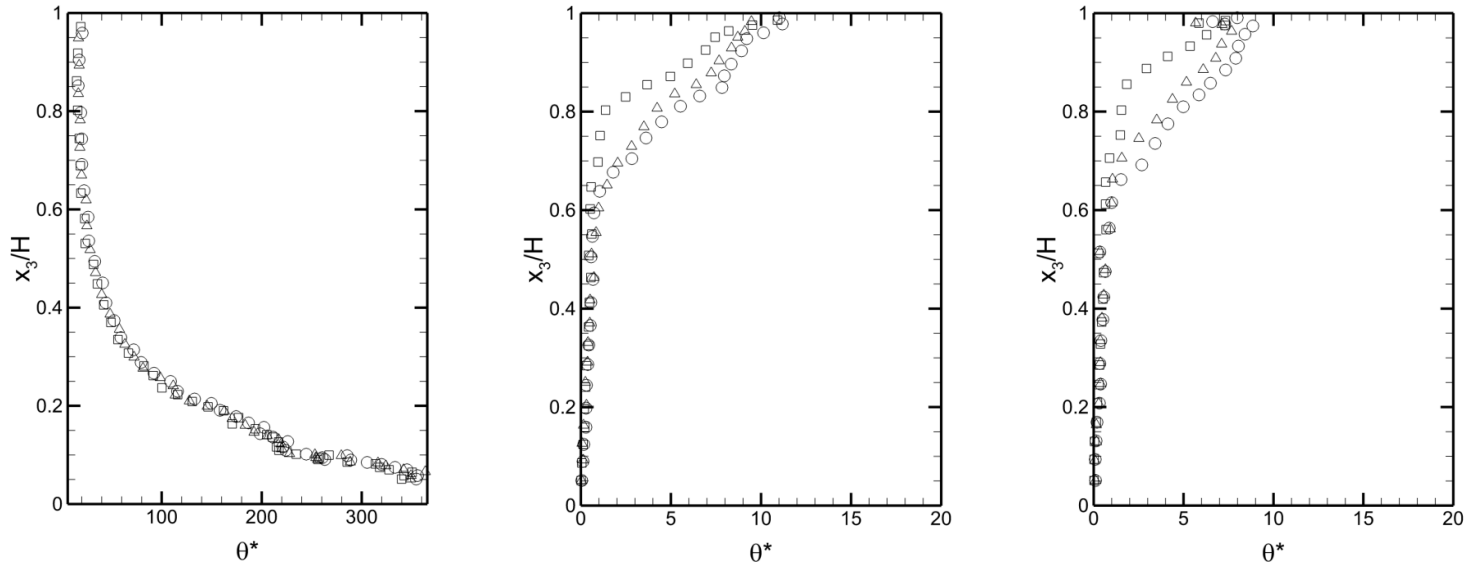

a) b) c)

Figure 21, θ vs. x_3/H for a) $x_1/H=0$; b) $x_1/H=0.75$, c) $x_1/H=1.25$. □ $t^*=3.7$, Δ $t^*=7.4$, ○ $t^*=14.8$; $m^*=1.25e\text{-}6$; ensemble averaged from 3 cases, time averaged over $t^*=0.3$.*

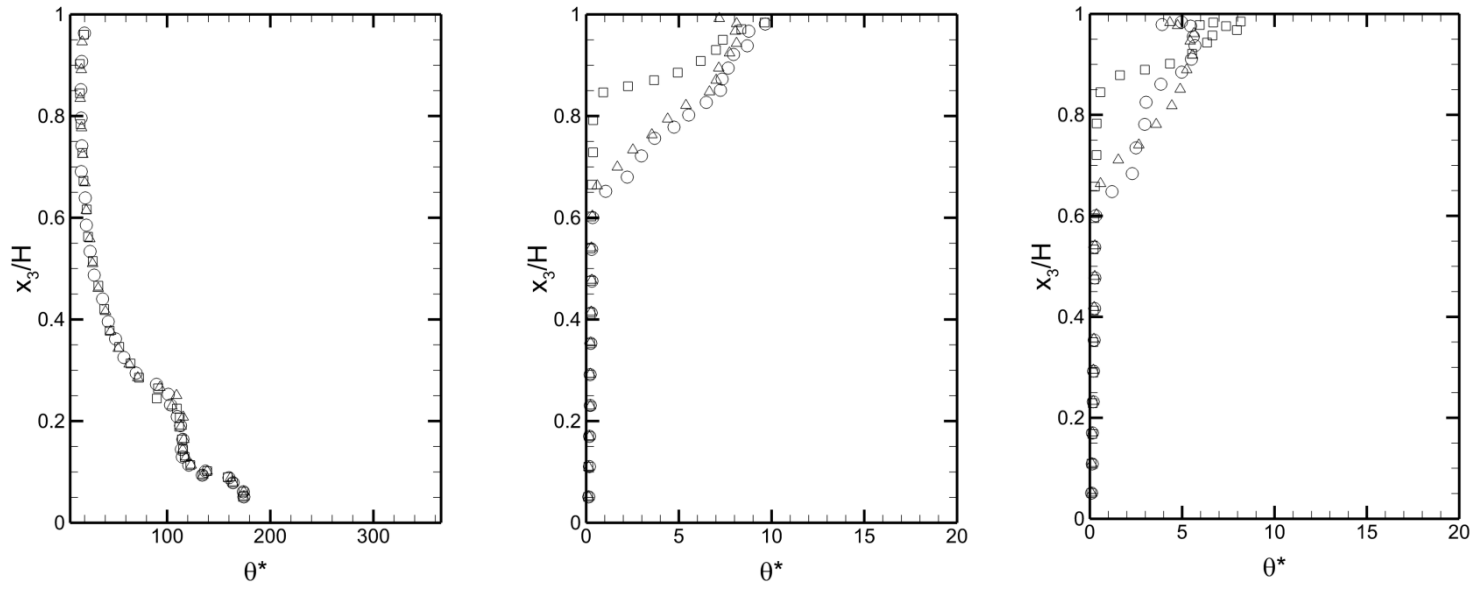

a) b) c)

Figure 22, θ vs. x_3/H for a) $x_1/H=0$; b) $x_1/H=0.75$, c) $x_1/H=1.25$. □ $t^*=3.7$, Δ $t^*=7.4$, ○ $t^*=10$; $m^*=2.5e\text{-}6$; ensemble averaged from 3 cases, time averaged over $t^*=0.3$.*

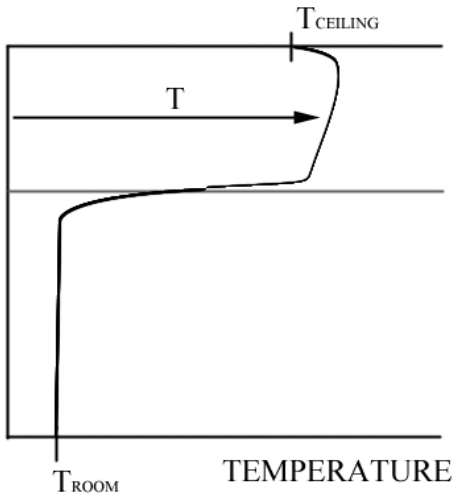

Figure 23, Temperature profile sketch from Zukoski for a smoke layer in an enclosure.

Zukoski's profile for a real fire ceiling layer shows a small gradient through the layer and a large gradient at the interface. This may indicate that the salt-water model ceiling layer is not as turbulent as that of a real fire with steep gradients. Mixing in both cases is driven by the Grashof number, which is calculated to be $8.9 * 10^{10}$ for these experiments, and on the order of $3.5 * 10^{15}$ for a full-scale fire. The transition point to turbulence is a Grashof number of 10^9, so the flow in the salt-water model turbulent gradients are not as large. Also, the density difference at the ceiling represents the adiabatic condition present for the salt-water experiments, where a real ceiling layer will have lower temperature at the ceiling due to heat transfer.

The density difference in the ceiling layer was also measured radially near the ceiling at a location of $x_1/H=0.93$, and is plotted in ***Figure 24*** and ***Figure 25***. ***Figure 24*** presents the density difference for the low flow case, with $m^*=1.25e\text{-}6$, and ***Figure 25*** shows the high flow case, with $m^*=2.5e\text{-}6$. The figures show that the radial profile for density difference is fairly constant between the plume and wall, decreasing

steadily towards the wall. For the higher flow tests, density difference was found to remain constant at later times, with the curves at t^*=7.4 and 10 about the same. The vertical profile in ***Figure 22*** confirms this behavior.

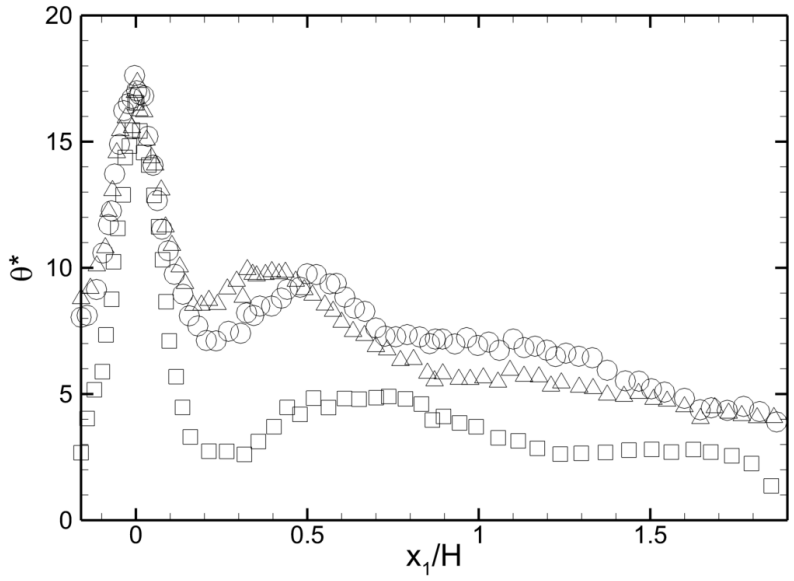

Figure 24, θ vs x_1/H for x_3/H=0.93. □ t^*=3.7, Δ t^*=7.4, ○ t^*=14.8; m^*=1.25e-6; ensemble averaged from 3 cases, time averaged over t^*=0.3.*

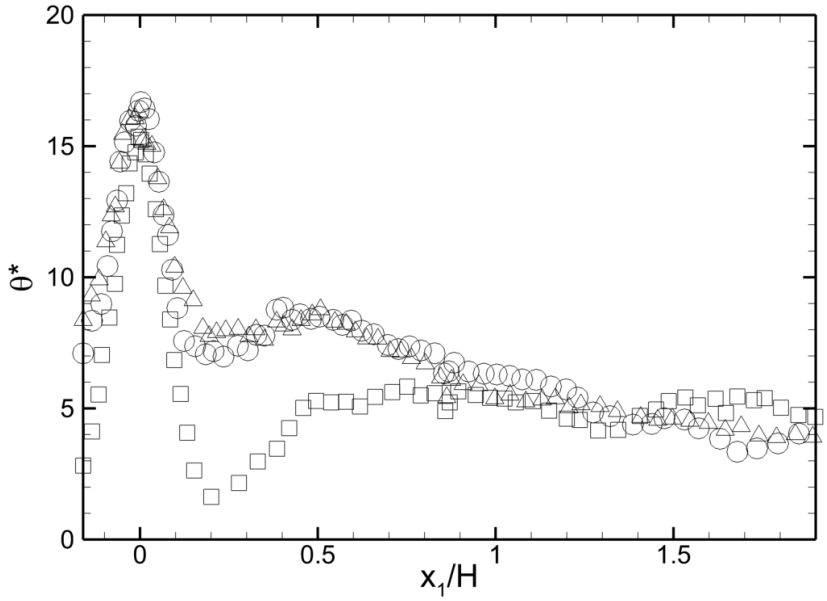

Figure 25, θ vs x_1/H for x_3/H=0.93. □ t^*=3.7, Δ t^*=7.4, ○ t^*=10; m^*=2.5e-6; ensemble averaged from 3 cases, time averaged over t^*=0.3.*

3.3 Transient Ceiling Layer Dynamics

Instantaneous and time averaged ceiling layer velocities were calculated using DaVis and were non-dimensionalized by a characteristic velocity, U_0, based on the dimensionless source strength, m^*. Length was non-dimensionalized by the enclosure height, *H*.

Instantaneous ceiling jet horizontal velocity profiles were measured and plotted in ***Figure 26*** and ***Figure 27***. Using the combined PIV and PLIF images, the velocity was plotted as a profile overlaid on a contour of the density difference. These combined measurements allow insight into velocity's relation to the smoke layer density. Velocity profiles were taken at the times where the ceiling jet reached x_1/H=0.25, 0.75, and 1.25. These profiles are measured at time t^*=3.7, when the initial ceiling jet reaches the wall and begins to turn back toward the plume. No averaging was performed for these images.

As the figures show, the ceiling jet velocity is higher when the ceiling jet is closer to the source, with a velocity of $u_1/u_0 = 2$ when r/H=0.5. From r/H=1 to r/H=1.5, u_1/u_0 remains constant at about 1.4. The density difference is clearly seen to be higher towards the ceiling, but does not show a consistent, direct correlation to velocity. Locations with high θ^* values do not necessarily have high velocity, as ***Figure 27a*** demonstrates.

Ceiling jet velocities close to the plume show a high velocity near the wall with intermittent negative velocity near the bottom of the ceiling jet. At this early point in

time, a steady flow towards the plume has not yet developed, with only slight negative velocity below the ceiling jet.

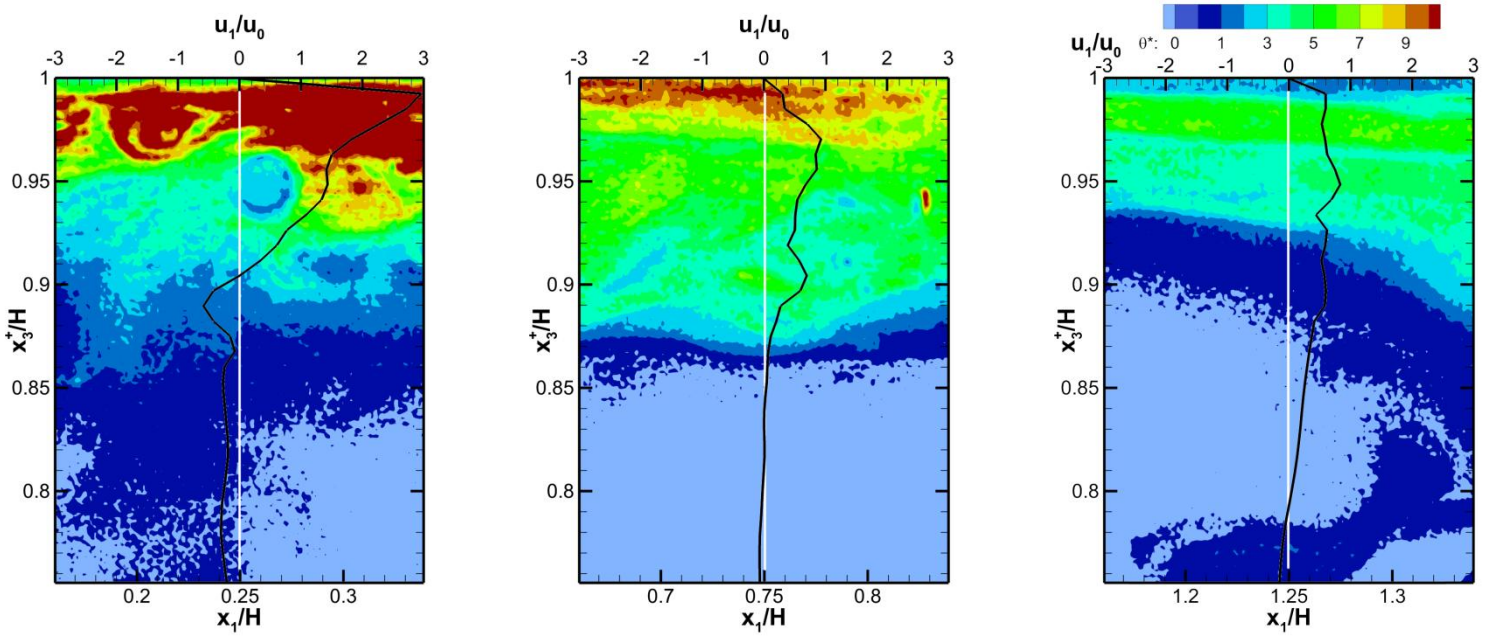

(a) (b) (c)

Figure 26, Early dimensionless ceiling jet velocity plotted over dimensionless density difference; m^*=1.25e-6, case 1.

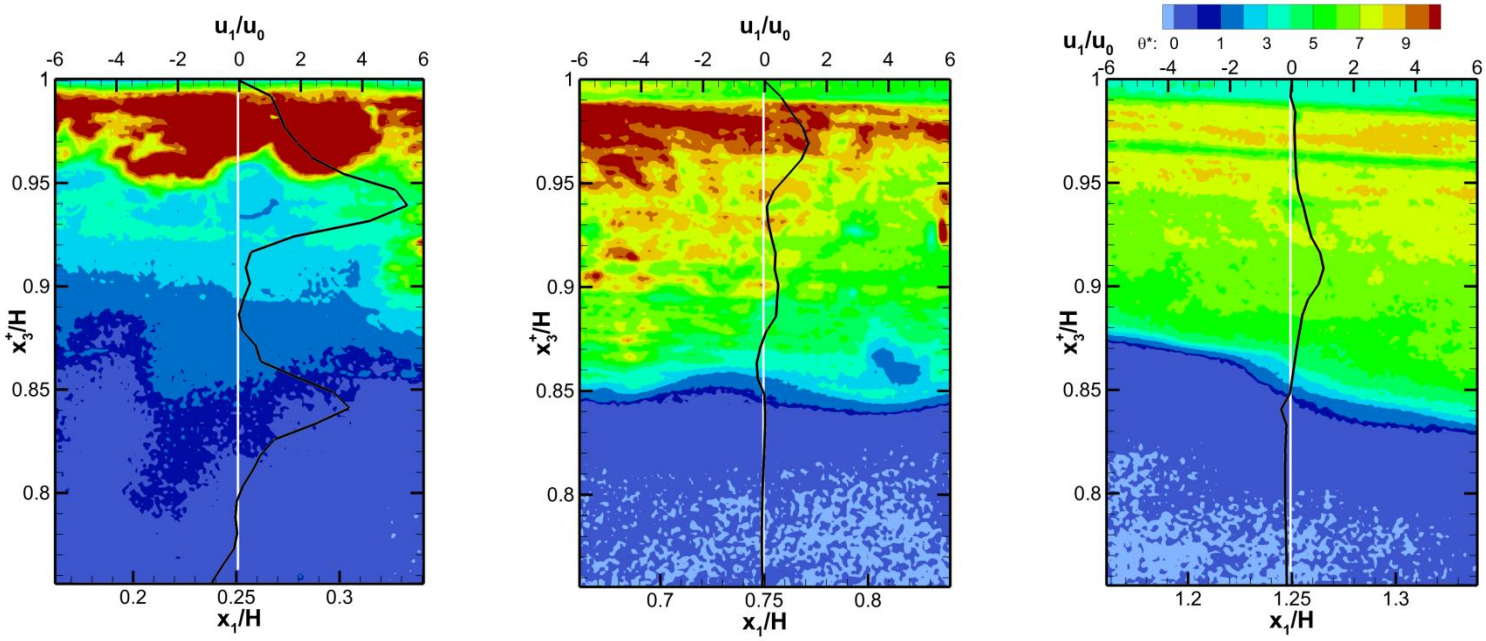

(a) (b) (c)

Figure 27, Early dimensionless ceiling jet velocity plotted over dimensionless density difference; m^*=2.5e-6, case 1.

Figure 28 shows the theoretical velocity profile within a steady-state smoke layer, given by Zukoski, and shows a high positive velocity in the upper half of the layer, followed by transition to a negative velocity in the lower half and fresh air/water.

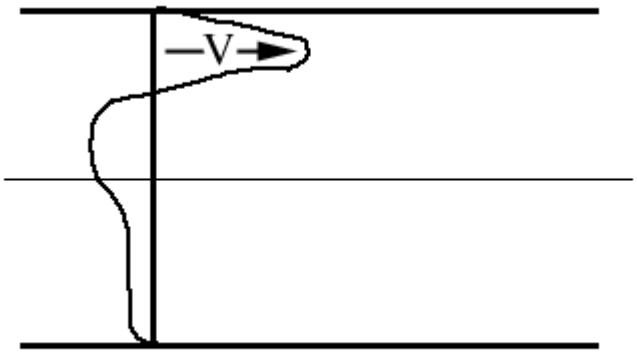

Figure 28, Qualitative theoretical velocity within the smoke layer, from Zukoski[44]

By using the combined PIV and PIV time-series technique, flows throughout the entire enclosure can be accurately analyzed. To show the overall flow within the enclosure, instantaneous ceiling layer velocities were measured at the dimensionless times t^*=3.7, 7.4, and 14.8, and are plotted in ***Figure 29 (a)***, ***(b)***, and ***(c)***, respectively. Vector lengths are uniform, and the contour shows the magnitude of the dimensionless velocity.

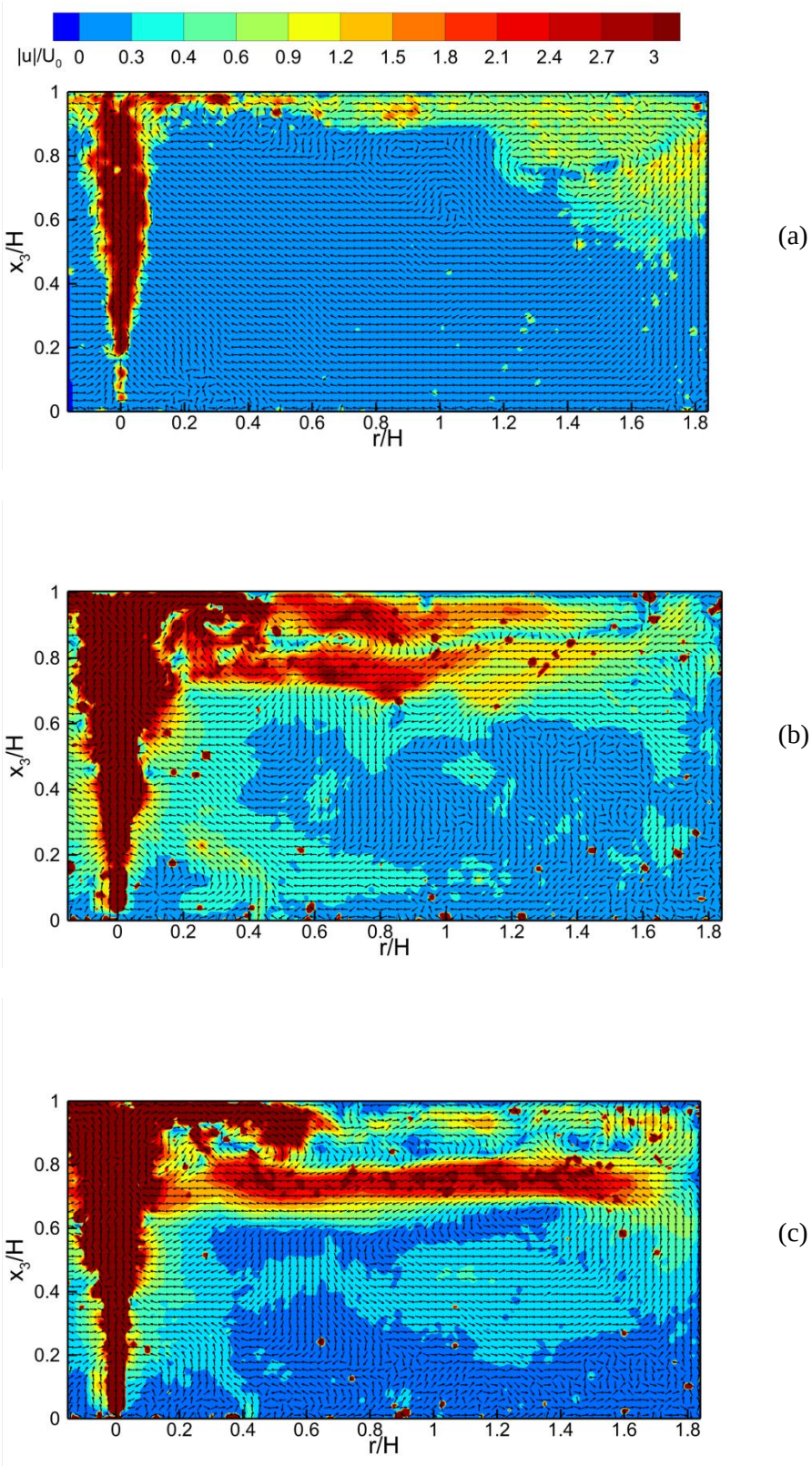

(a)

(b)

(c)

Figure 29, Instantaneous velocity at (a) t=3.7, (b) t*=7.4, and (c) t*=14.8; m^*=1.25e-6, case 1.*

As ***Figure 29a*** shows, the early ceiling jet is turbulent and has circular mixing regions at x_1/H=0.2 and x_1/H=1.4. The mixing at x_1/H=0.2 is due to the turning of the flow as it hits the ceiling and transitions into the ceiling jet. This mixing is only present at early times and, as the ceiling layer further develops, the circular flow moves to r/H=0.4. This can be seen more clearly in ***Figure 30***, which shows late time-averaged behavior of the plume over 100 frames, around t^*=14.8.

Figure 29b & ***c*** and ***Figure 30*** show that the velocities behave as Zukoski[44] described in ***Figure 28***, where the flow is moving toward the wall in the top half of the layer, and transition toward the plume in the bottom half. ***Figure 30*** includes streamlines to better illustrate the flow path of steady-state confined flow. Flow near the injector does not move parallel to the enclosure floor due to the openings near the injector.

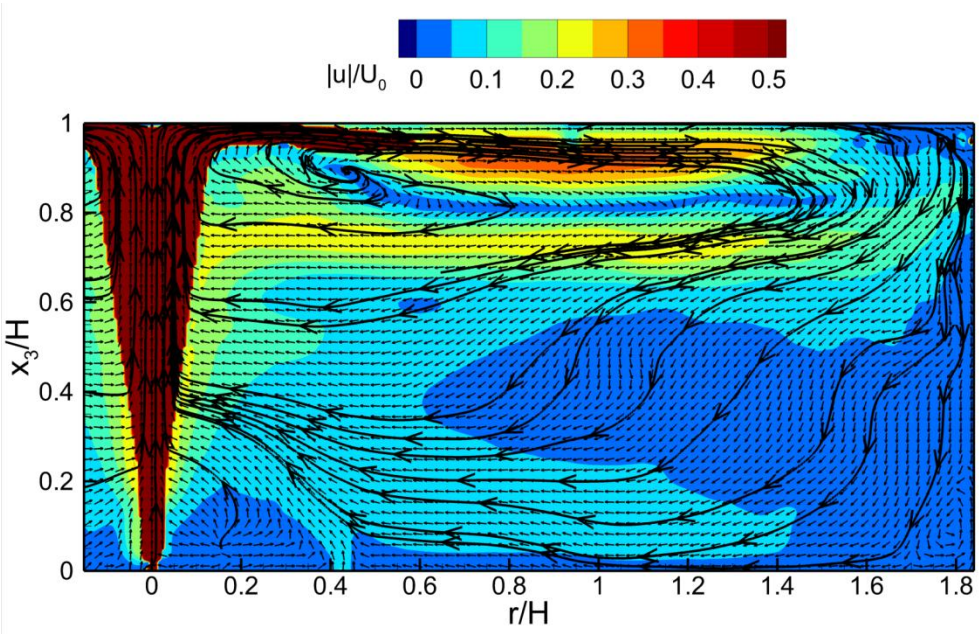

Figure 30, Late-time (t=10) velocity streamlines plotted over dimensionless density difference; m^*=1.25e-6, case 1; time-averaged over t^*=1.5.*

3.4 Mass Entrainment

With the ability to measure both density and velocity, the simultaneous PIV and PLIF measurements were used to calculate mass flux and mass entrainment. Mass flux was found by converting the θ measurements from the unconfined plume into density and, multiplying by u_3.

$$\dot{m}''_{ent} = \rho_{sw} u_3$$

This was then integrated radially around the plume centerline to find the mass entrainment rate as a function of height above the plume.

$$\dot{m}_{ent} = 2\pi \int x_1 (\rho_{sw} u_3)_{mean} dx_1$$

This function was then non-dimensionalized by $\rho_0 g^{1/2} (D^*)^{3/2}$.

Because the density difference between the fresh water and salt-water was small, ambient flows within the fresh water had the potential to affect these measurements, growing exponentially with radial distance from the plume. To eliminate the effect of ambient flow velocity on mass entrainment rate, a threshold density was set such that, when integrating, velocity was set to zero where density was less than double the magnitude of the noise for the ambient flow. This provided a good approximation of the mean plume boundary, where it was safe to assume no flow was being entrained into the plume. *Figure **31*** shows instantaneous and mean contour plots of the mass flux into the plume for the unconfined configuration.

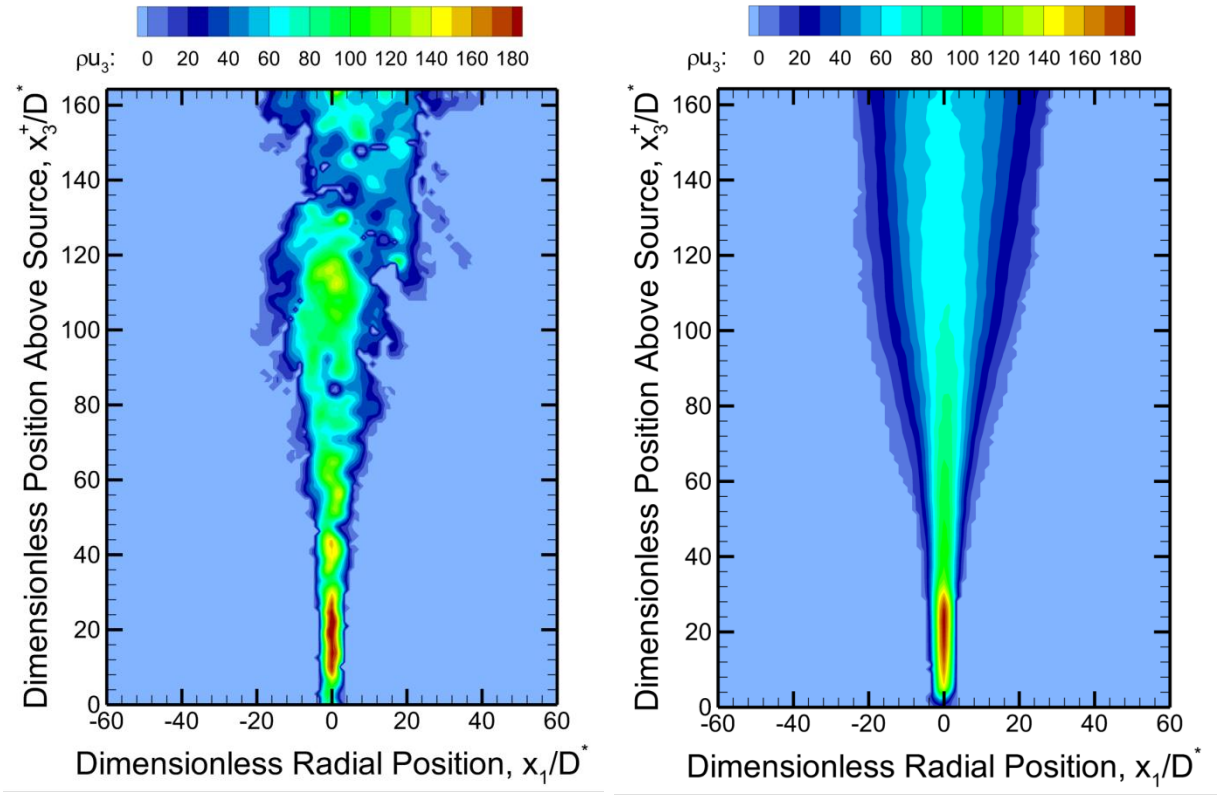

(a) (b)

Figure 31, Instantaneous (a) and mean (b) contours of mass flux; unconfined plume.

Figure 32 shows the result of integrating for mass entrainment rate as a function of vertical position above the source, plotted on a logarithmic scale. A clear linear curve is established for the plume beginning around x_3/D^*=60.

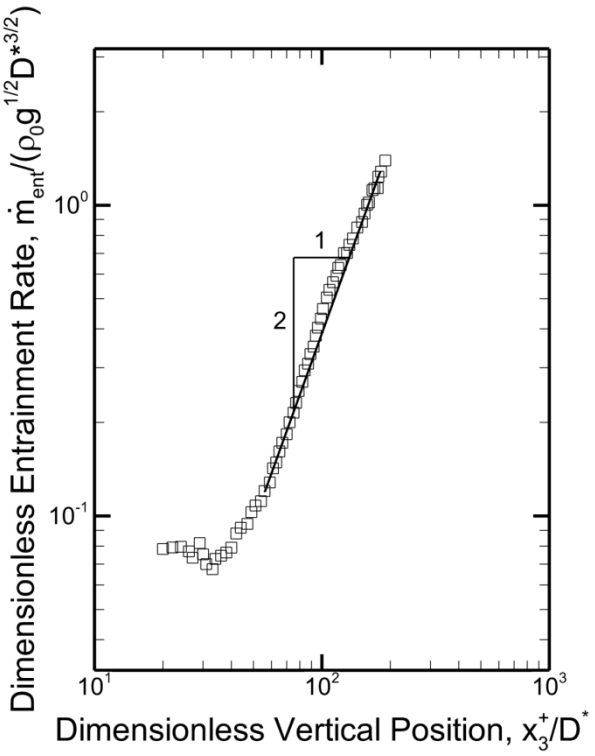

Figure 32, Dimensionless mass entrainment rate as a function of height above the source.

3.5 Subgrid-Scale Mixing Analysis

With the very high resolution measurements made possible using PLIF, an analysis was made into how image resolution affects measurements of turbulent mixing. A MATLAB program was written to scale images down to a smaller resolution by spatially averaging over cells, while also storing the original data. ***Figure 33a*** shows one instantaneous image scaled down, with the 32x32 cell grid overlaid above the location of each cell. ***Figure 33b*** shows a close-up of the data from one 32 pixel wide cell, located along the centerline and at a height of z/D^*=29. In this case, 32 pixels correspond to a dimension of 1.4 D^*.

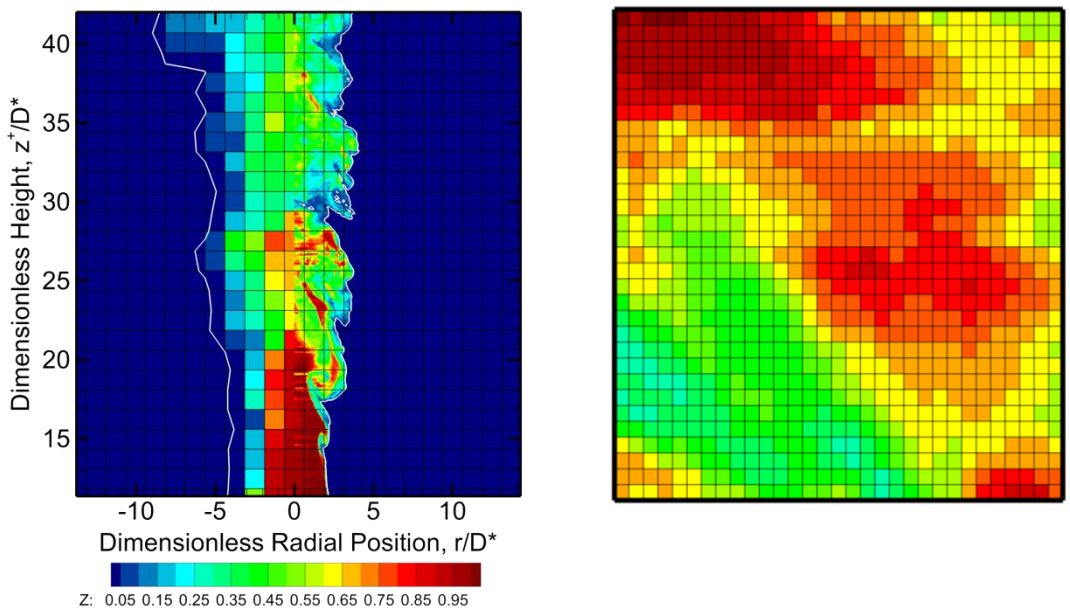

(a) (b)

Figure 33, (a) Instantaneous PLIF image with and without spatial averaging (left and right half), with mixture fraction of 0.05 outlined, and (b) close-up of 1.4 D^* wide cell along centerline at z/D^* of 29.

The figure also shows an outline of the location where the mixture fraction is 0.05, as an approximation of the location of a flame. Though salt-water modeling cannot model the flame or intermittent region of a fire, the measurements can still provide insight into mixing and other properties. The figure shows that decreasing the resolution by a factor of 1.4 D^* moves the flame front 1 D^* away from the plume centerline. This is because the mixture fraction gradient is much larger with a lower resolution.

Figure 18 measured the loss of fidelity with resolution, showing the standard deviation of cell mixture fraction along the centerline as the images were scaled to smaller resolutions. No significant changes were observed until the resolution was below 0.6 D^*, at which point the maximum standard deviation increased

exponentially. Based on these results, a smaller cell size of approximately 0.6 D^* should be explored in future analysis into this subject.

Figure 34 compares various statistics for the PLIF measurements over the 32 pixel cell in ***Figure 33b***. The 3D landscape plot shows the probability density function (PDF) of the mixture fraction for the cell at $z^*=29.4$ and $r/D^*=0$, over a time of 6τ. This plot was found by creating a histogram for the cell and comparing to the mean values averaged over space and time for that cell, as well as the total standard deviation of mixture fraction within the cell. The histogram was then converted from a probability mass function to a probability density function. The PDF fluctuates over time from the turbulent flow, as pockets of higher and lower salt concentration pass through the cell. If the camera frame rate was higher, the peaks of data would appear to transition better between time steps, but at the maximum 7Hz frame rate of the hardware the flow would typically move out of the cell by the time the next image was recorded. With a flow velocity of around 0.15 m/s, a frame rate of 43 Hz would be required to keep half the flow in a 32x32 cell between two frames.

The time-averaged PDF over the 300 images taken is a Gaussian curve with a slight positive bias, and is shown adjacent to the instantaneous PDF. Plotted above the PDF is the temporal and spatial standard deviation of mixture fraction for the cell for each image, with the overall standard deviation plotted as a single line. Standard deviation is normalized by the temporal and spatial average of the mixture fraction. The gold colored dot shows the spatial average for the cell at that instant in time in ***Figure 33*.**

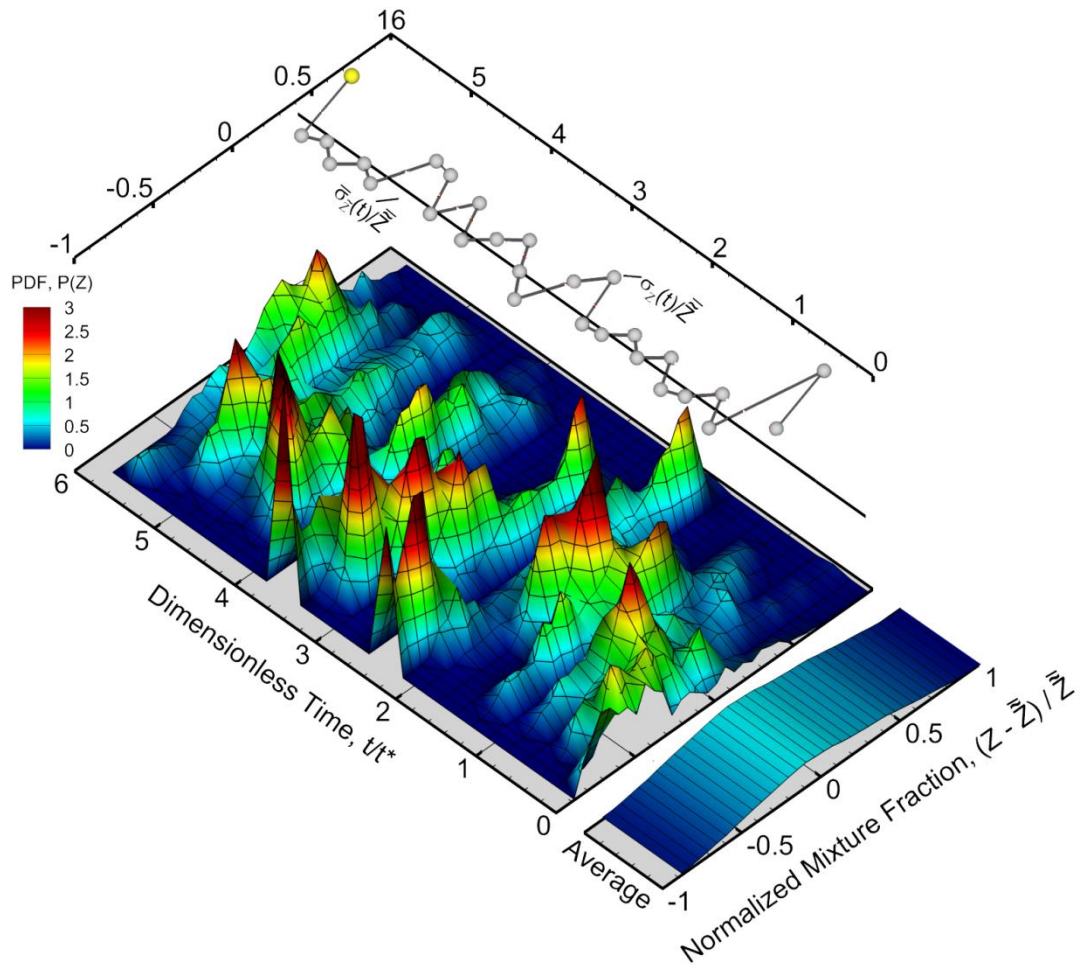

Figure 34, PDF of mixture fraction in a cell along the plume centerline over time, unconfined PLIF only case.

The overall value for $\sigma_Z/\tilde{\bar{Z}}$ for this cell was found to be 0.38, or 38%. Yao measured a standard deviation of about 41%, while Shabbir and George's correlation predicted a fluctuation of 40% at the fully developed turbulent region. Previous measurements by George et al.[34] found this value to be 38%, in very good agreement with the experimental results of this project. Nakagome and Hirata[35] found this value to be 43%, and Kotsovinos[37] found it to be 44%, all showing good agreement between theory and experimental results. Even with a cell size of twice the value of 0.6 D^*,

the standard deviation was calculated within an acceptable range, indicating that while 0.6 D^* may be the optimal limit for LES averaging, cell sizes up to 1.4 D^* may still be accurate.

Chapter 4: Conclusions

This study successfully validated salt-water modeling as an effective diagnostic tool for enclosure smoke filling, showing excellent agreement with both experimental data and theoretical data, as well as showing good repeatability between experiments.

A technique was developed that allows for combined PIV and PLIF measurements without sacrificing fidelity. A length scale was developed for spatial averaging based on analysis of turbulent fluctuation measured when scaling images to lower resolutions, and was found to be 0.6 D^*. A maximum fire size relative to room height of $z > 0.12\ (\dot{m}_{sw})^{2/5}$ was established based on where the plume region begins and intermittent flame region ends according to McCaffrey's results.

A method for taking PIV measurements of flows with a very wide range of velocities was developed by the use of combined PIV and PIV time-series post-processing, using a carefully selected time step to resolve all flow velocities. This allowed accurate measurement of velocities between 0.41 m/s and 0.00017 m/s for the field of view used in these experiments. Camera and laser setup and calibration procedures were carefully examined and refined to produce clean and accurate results.

Ceiling layer velocity was measured in high detail. Instantaneous patterns were measured and plotted over various times, noting locations of vortices and positive/negative flow velocities. Late-time streamlines were used to further illustrate flow patterns in the enclosure. The combined PIV and PIV time-series measurements allowed the entire range of flows within the enclosure to be analyzed simultaneously.

The combined measurements allowed comparison of velocity with density measurements at the same instant. Combined measurements were also used to calculate plume mass flux and mass entrainment rates.

An analysis was made into the turbulent mixing of the plume by scaling PLIF measurements and analyzing statistics of the measured mixture fraction. A probability density function of mixture fraction for a cell along the centerline was created, and the intensity of turbulent fluctuations was calculated. This mean intensity was found to agree well with data from multiple previous full-scale experiments and analyses of theory, showing that these diagnostic techniques are an excellent tool for insight into this behavior.

Further work in succession to this project may include:

-Incorporating variable salt-water flow rates to simulate t^2 fires.

-Working to reduce reflections in the enclosure PLIF data.

-Performing analysis of ambient flow in the large tank to improve on measurements of the unconfined plume.

-Performing analysis into why the virtual origin and constant of proportionality for unconfined plume velocity data are inconsistent between experiments.

-Extending analysis of turbulent fluctuation and dependence on grid scale resolution, using a setup with higher recording rate.

Bibliography

[1] *R.L. Alpert, "Fire Induced Turbulent Ceiling-Jet," Factory Mutual Research Corporation, Norwood MA, FMRC Serial No.19722-2, pp 35(1971).*

[2] *R.L. Alpert, "Calculations of Response Time of Ceiling Mounted Fire Detectors" Fire Technology, 8, 3, pp 181-195 (1972).*

[3] *G. Heskestad, "Physical Modeling of Fire," Journal of Fire & Flammability, 6, p. 253 (1975).*

[4] *G. Heskestad, "Generalized Characteristics of Smoke Entry and Response for Products-of-Combustion Detectors," in Proceedings, 7th International Conference on Problems of Automatic Fire Detection, Rheinish-Westfalischen Technischen Hochschule, Aachen, Germany (1975).*

[5] *Cooper, L. Y., Harkleroad, M., Quintiere, J., and Rinkinen, W. (1981). An experimental study of upper hot layer stratification in fuel scale multiroom fire scenarios, ASME 81-HT-9, Milwaukee.*

[6] *Zukoski, E.E., and Kubota, T. (1980). Two layer modeling of smoke movement in building fires, Fire Mat. 4, 17.*

[7] *Mitler, H. E., and Emmons, H. W. (1981). Documentation for CFC V, The fifth Harvard computer fire code, Home Fire Project Tech. Rep. No. 45, Harvard University, Cambridge, MA.*

[8] *S.P. Jankiewicz "Predicting Smoke Detector Response Using a Quantitative Salt-Water Modeling Technique", M.S. Thesis, Dept. Fire Protection Engineering, University of Maryland, College Park (2004)*

[9] *Chan, C.S., "Characterizing Smoke Dispersion Along Beamed Ceilings Using Salt-Water Modeling," M.S. Thesis, Dept. Fire Protection Engineering, University of Maryland, College Park, MD (2010).*

[10] *J.G. Quintiere, "Scaling Applications in Fire Research", Fire Safety Journal, 15: p. 3-29 (1989).*

[11] *Yao, X., 2006, Characterization of Fire Induced Flow Transport Along Ceilings Using Salt-Water Modeling. Dissertation for Ph.D, Dept of Fire Protection Engineering, University of Maryland.*

[12] *Heskestad, G.,"Physical Modeling of Fire," J. of Fire & Flammability, 6, p. 253 (1975).*

[13] *Heskestad, G., "Engineering Relations for Fire Plumes," Fire Safety Journal, Vol 7, 25-32 (1984)*

[14] *Beyler, C.L., "Fire Plumes and Ceiling Jets," Fire Safety Journal 11, 53-75 (1986).*

[15] *Zukoski, E.E., "Combustion Fundamentals of Fire." (1995)*

[16] *Faeth, G.M., and You, H.Z., "An Investigation of Fire Impingement on a Horizontal Ceiling," Report for U.S. Department of Commerce and National Bureau of Standards, (1979)*

[17] *Alpert, Ronald L., Ceiling Jet Flows, SFPE Handbook of Fire Protection Engineering, Third Edition, 02-02. (2002)*

[18] *Zukoski, E.E., Development of a stratified ceiling layer in the early stages of a closed-room fire, Fire and Materials, 1978, 2, 54-62*

[19] *Hagglund et al., "Smoke Filling Experiments i n a 6 x 6 ~ 6 Meter Enclusure," FOA Repport C20585-D6, Forsvarets Forskningsanstalt, Stockholm, September 1985.*

[20] *Hurley, M. "ASET-B: Comparison of Model Predictions with Full-scale Test Data," NIST, January 2002.*

[21] *Cooper, L. Y., Harkleroad, M., Quintiere, J., and Rinkinen, W. (1981). An experimental study of upper hot layer stratification in fuel scale multiroom fire scenarios, ASME 81-HT-9, Milwaukee.*

[22] *Zukoski, E.E., and Kubota, T. (1980). Two layer modeling of smoke movement in building fires, Fire Mat. 4, 17.*

[23] *Thomas, P.H., Hinkley, P.L., Theobald, C.R. and Simms, D.L., (1963) "Investigations into the Flow of Hot Gases in Roof Venting," Fire Research Technical Paper No. 7, HMSO, London.*

[24] *Tangren, E. N., Sargent, W. S. and Zukoski, E. E., (1978) "Hydraulic and Numerical Modeling of Room Fires," California Institute of Technology, Pasadena, California.*

[25] *Zukoski, E.E, (1978) "Prediction of Smoke Movement in Buildings," California Institute of Technology, Pasadena, Ca.*

[26] *K.D. Steckler, H.R. Baum, and J.G. Quintiere, " Salt Water Modeling of Fire Induced Flows in Multi-Compartment Enclosures," NBSIR 86-3327, Gaithersburg, MD: National Bureau of Standards (1986).*

[27] *McCaffrey, B.J., Purely Buoyant diffusion Flames: Some Experimental Results. Center For Fire Research, 1979.*

[28] *Alpert, R.L., Turbulent Ceiling-Jet Induced by Large-Scale Fires. Combustion Science and Technology, 1971.* ***11****: p. 197-213.*

[29] *E.L. Young "Wind-driven Plume Dispersion Near a Building", M.S. Thesis, Dept. Fire Protection Engineering, University of Maryland, College Park (2008)*

[30] *Webster, D.R., Roberts, P.J.W., and Ra'ad, L., Simultaneous DPTV/PLIF measurements of a turbulent jet, Experiments in Fluids 30 (2001).*

[31] *Lipp, C.W., et al., Measurement of Reactive Mixing of Liquids with Combined PIV and Reactive PLIF Methodology, Process Mixing Group, Dow Chemical Company.*

[32] *Shimura, M. et al., Simultaneous dual-plane CH PLIF, single-plane OH PLIF and dual-plane stereoscopic PIV measurements in methane-air turbulent premixed flames, Proceedings of the Combustion Institute, Vol 33 Issue 1 (2011).*

[33] *Shabbir, A. and George, W., "Experiments on a Round Turbulent Buoyant Plume," J. Fluid Mech., 1-32 (1994)*

[34] *George, W.K., Jr., Alpert, R.L., Tamanini, F. "Turbulence measurements in an axisymmetric buoyant plume," Int. J. Heat Mass Trans. 20, 1145-1154 (1977)*

[35] *Nakagome, H. and Hirata, M., "The structure of turbulent diffusion in an axisymmetrical thermal plume," Heat Trans. & Turbuletn Buoyant Convection, (Spalding and Afgan, eds.) McGraw-Hill, NY. 367-372 (1977)*

[36] *Papanicolaou, P.N. and List, E.J., Statistical and Spectral Properties of tracer Concentration in Round Buoyant Jets." Int. J. Heat Mass Transfer, 30, 2059-2071 (1987)*

[37] *Incropera, F.P., and Dewitt, D.P., Fundamentals of Heat and Mass Transfer, ed. S. Edition. New York: John Wiley & Sons (1985)*

[38] *A.A. Kelly, "Examination of Smoke Movement in a Two-Story Compartment Using Salt Water and Computational Fluid Dynamics Modeling," M.S. Thesis, Dept. Fire Protection Engineering, University of Maryland, College Park, MD (2001).*

[39] *Larsen LG, Crimaldi JP, The effect of photobleaching on PLIF exp. Fluids (2006)*

[40] *Adrian, R. and Westerweel, J., "Particle Image Velocimetry," Cambridge University Press (2011)*

[41] *Keane, R. and Adrian, R, Optimization of particle image velocimeters. Part I: Double pulsed systems, Meas. Sci. Technol. 1, 1202-1215 (1990)*

[42] *Zukoski, E.E., Development of a stratified ceiling layer in the early stages of a closed-room fire, Fire and Materials, 1978, **2**, 54-62.*

[43] *Quintiere, J., "Fundamentals of Fire Phenomena," John Wiley & Sons. (2007)*

[44] *Zukoski, E.E., "Combustion Fundamentals of Fire." (1995)*

[45] *Heskestad, G., "Fire Plumes, Flame Height, and Air Entrainment," SFPE Handbook of Fire Protection Engineering, Third Edition, 02-29. (2002)*

[46] *Kingori, G., "ENFP 429 Independent Study, Salt-Water Modeling," University of Maryland Fire Protection Engineering (2010)*